Efficient overall water splitting of suspended photocatalyst boosted by metal-support interaction

Yu Qi,[1] Boyang Zhang,[2] Guanhua Zhang,[3] Zhaoke Zheng,[4] Tengfeng Xie,[5] Shanshan Chen,[6] Guijun Ma,[2] Can Li,[1] Kazunari Domen[6] and Fuxiang Zhang[1,7]*

[1] State Key Laboratory of Catalysis, Dalian Institute of Chemical Physics, Chinese Academy of Sciences, Dalian National Laboratory for Clean Energy; Dalian, 116023, P. R. China.

[2] School of Physical Science and Technology, ShanghaiTech University; Shanghai 201210, China.

[3] State Key Lab Molecular Reaction Dynamic, Dalian Institute of Chemical Physics, Chinese Academy of Sciences, Dalian 116023, P.R. China.

[4] State Key Laboratory of Crystal Materials, Shandong University; Jinan 250100, China.

[5] College of Chemistry, Jilin University; Changchun, Jilin 130012, China.

[6] Research Initiative for Supra-Materials (RISM), Shinshu University; Nagano 380-8553, Japan; Office of University Professors, The University of Tokyo; Tokyo 113-8656, Japan.

[7] Lead Contact

*Correspondence: fxzhang@dicp.ac.cn (F.Z.)

SUMMARY

Strong metal-support interaction (SMSI) has been widely discussed for activity promotion of heterogeneous catalysis, but it remains unclear for photocatalysis. Here we employ bismuth vanadate ($BiVO_4$) supported iridium (denoted as Ir/BVO) as a model photocatalyst to observe highly dispersed iridium overlayers as well as moderate SMSI effect between Ir and $BiVO_4$. It is revealed that charge separation on the Ir/BVO can be remarkably promoted by the SMSI effect. Together with right distribution of dual cocatalysts (Ir and IrO_2) achieved by a simple photoinduction, the water oxidation activity on optimal Ir/BVO is about 75 times of magnification with respect to the pristine BVO. Finally, we construct an effective redox-driven Z-scheme overall water splitting system with a benchmarking apparent quantum efficiency of 16.9% under visible light irradiation of 420 ± 10 nm at room temperature. Our work extends application territory of SMSI into photocatalysis to provide alternative way of promoting photocatalytic activity.

KEYWORDS: photocatalysis, overall water splitting, metal-support interaction, hydrogen, charge separation

INTRODUCTION

Strong metal-support interaction (SMSI) in supported metal catalysts has been extensively reported for remarkable promotion on various heterogeneous catalysis[1-5] One of its merits is to modify the interface between metal and support for efficient electron transfer as well as structural modulation of the active sites to remarkably promote the activity[3,6]. The SMSI concept has been early demonstrated in the platinum group metals supported on reducible oxides such as TiO_2, Fe_3O_4 and CeO_2[1,7,8]. To date, its territory has been widely extended into other metals (i.e., Au, alloys, single-atom metals) and inert/conducting supports (i.e., phosphates, hydroxides, conducting carbon and carbides etc.)[9-14]. To our knowledge, however, it still remains unclear whether territory of the SMSI concept can be further extended into the supported metal photocatalyst (also called as metal supported photocatalyst) for promotion of solar-to-chemical conversion.

Supported metal photocatalyst is one of the most typical supported metal catalysts, which has been extensively employed for suspended powder-based heterogeneous photocatalytic water splitting or carbon dioxide reduction to produce solar fuels such as hydrogen and methanol[15-20]. Different from conventional thermal-catalysis, the photocatalysis involves photo-absorption and charge separation of photogenerated carriers in addition to surface catalysis[19]. Meanwhile, the loaded metal, generally called as the cocatalyst of the metal supported photocatalyst, has been known to own functionalities of promoting both charge separation and surface catalysis[21]. It has also been demonstrated that the intimate interface between the semiconductor support and metal cocatalyst is extremely favorable for the interfacial charge separation as well as photocatalytic activities[22,23]. In this case, it renders us to reasonably wonder whether the interfacial charge separation and photocatalytic overall water splitting (OWS) activity on the supported metal photocatalysts can be also promoted by the SMSI.

Monoclinic bismuth vanadate ($BiVO_4$, denoted as BVO hereafter) is one of the most popularly discussed visible-light-responsive O_2-evolving photocatalysts[24-30]. Recently, we have demonstrated that the metallic Ir loaded on the BVO is highly active as the cocatalyst for the reduction of $[Fe(CN)_6]^{3-}$ as well as Z-scheme OWS[28]. Here, both Ir cocatalyst and BVO semiconductor are thus chosen to construct the metal/semiconductor support interface for model discussion on the metal-support interaction effect. We find that a moderate SMSI exists in the semiconductor BVO supported iridium (Ir/BVO) photocatalyst, which is first experimentally confirmed to make a remarkable promotion on the interfacial charge separation as well as photocatalytic water splitting performance. The water oxidation activity of optimal Ir/BVO photocatalyst is enhanced by 75 times with respect to the pristine BVO, and through employing it as the O_2-evolving photocatalyst (OEP), the redox-driven Z-scheme OWS system was constructed together with H_2-evolving photocatalyst (HEP) and $[Fe(CN)_6]^{3-/4-}$ redox mediator. We achieve stoichiometric H_2 and O_2 evolution with a benchmarking apparent quantum efficiency (AQE) of 16.9% at 420 ± 10 nm and solar-to-hydrogen (STH) efficiency of 0.8% under one-sun illumination in the suspended solution at room temperature.

RESULTS

Identification of moderate SMSI effect

The monoclinic BVO with exposed {010} and {110} facets was synthesized by hydrothermal method (Figure S1), on the surface of which the iridium precursor was then randomly deposited through the impregnation method and reduced at the temperature region of 473–673 K under the flow of 5 *vol*% H_2/Ar. The obtained samples are correspondingly denoted as Ir/BVO-n (“n” represents the reduction temperature). As for discussion, photo-deposition of iridium at room temperature was carried out to obtain the Ir/BVO-PD named sample free of the SMSI effect.

The actively moderate SMSI effect is observed in our prepared Ir/BVO-573 and Ir/BVO-673 photocatalyst based on the following facts: (1) the deposited Ir nanoparticles remain dispersed on the surface of semiconductor BVO with a thin layer covered (Figure 1A and Figure S2), and the thin layer will disappear after the O_2/Ar oxidation treatment (Figure S3). (2) remarkable electron transfer from BVO to the deposited metallic iridium is observed by comparing their Ir 4*f* binding energies with that of Ir/BVO-PD (Figure 1B). (3) the peak belonging to CO adsorption on the Ir metal is observed on the Ir/BVO-473 sample, but disappears for Ir/BVO-573 and Ir/BVO-673 samples (Figure 1C) due to the existence of nanolayer on the Ir nanoparticles. The schematic diagram of SMSI over the Ir/BVO-n samples is simply described in the inset of Figure 1C. It is worth noting that here the deposited Ir nanoparticles on the Ir/BVO-573 and Ir/BVO-673 samples are aggregated with increasing reduction temperature (Figure 1A and Figure S2), demonstrating the SMSI is relatively moderate. This should result from the low work function of Ir metal and/or the weak reducibility of BVO. It is also worthy of being mentioned that no SMSI should exist in the Ir/BVO-473 sample due to the similar shortage of thin covering layer (Figure S4) and its similar binding energy as that of Ir/BVO-PD free of thermal treatment as well as the SMSI (Figure S5).

Controllable conversion of dual cocatalysts by photoinduction

Photoinduction was carried out to rationally convert the randomly impregnated iridium species (Ir, IrO_2) into controllable metallic Ir and IrO_2 cocatalysts on the corresponding {010} and {110} facets of BVO for the purpose of fabricating efficient redox-driven Z-scheme OWS as illustrated in Figure 2A. Meanwhile, the photoinduced Ir on the {010} facet and IrO_2 on the {110} facet of BVO are expected as selectively deposited dual cocatalysts to make a better promotion on the charge separation as well as O_2-evolving activity of BVO with respect to the sample with the dual cocatalysts randomly deposited[31]. Above expectation is highly feasible and reasonable according to our previous reports: (1) spatial separation of photogenerated electrons and holes among different facets of BVO happens during photoirradiation to cause the accumulation of photogenerated electrons and holes on the {010} and {110} facets, respectively[25]. (2) the metallic Ir is favorable for the electron transfer and the reduction of $[Fe(CN)_6]^{3-}$ [28], while the IrO_2 has been widely reported to promote hole transfer and activation of water oxidation[32,33]. The corresponding evolution of iridium species during the photoirradiation could be described as Figure 2B, where the photoreduction of IrO_2 into metallic Ir only happens on the electrons-accumulated {010} facets, while the photooxidation of metallic Ir into IrO_2 just proceeds on the holes-enriched {110} facets of BVO. Besides the spatial separation of photogenerated electrons and holes among the {010} and {110} facets of BVO, the selective photoinduced conversion also greatly benefits from the feature of photocatalysis that only photogenerated electrons can be used for reduction, while holes can be just used for the oxidation process. The photoinduced samples are correspondingly denoted as Ir(P.I.)/BVO-n for convenient discussion.

The oxidation of metallic iridium on the {110} facets of BVO during the photoinduction was experimentally confirmed by the emergence of IrO_2 species[34] on the Ir(P.I.)/BVO-673 compared to the Ir/BVO-673 with metallic iridium only detected (Figure 2C), in consideration of the fact that the oxidation of iridium species can only happen on the holes-accumulated {110} facets. In contrast, the reduction of iridium species on the {010} facets of BVO during the photoinduction can be revealed by results of *in situ* spatially resolved X-ray photoelectron spectroscopy (XPS) analysis on the specific {010} facet of single Ir/BVO-573 particle, which was achieved by connecting low energy electron microscopy (LEEM) with element chemical-state-specific X-ray photoemission electron microscopy (XPEEM) (Figure S6) to focus the measurement on the {010} facet. It was found that the IrO_2 species on the {010} facet of BVO under dark have been effectively converted into metallic iridium[34] after the 515 nm laser irradiation according to the obviously shifted binding energy (Figure 2D). Another evidence to support the structural evolution of deposited iridium species during photoirradiation is that the content ratio of Ir and IrO_2 species on the Ir/BVO-573 or 473 sample after the photoinduction is remarkably changed with respect to them without photoirradiation

(Figure S7 and Table S1).

Charge separation promotion based on SMSI and dual cocatalysts

Promotion of photoinduced Ir and IrO_2 dual cocatalysts on the charge separation of Ir/BVO photocatalysts can be remarkably observed and evidenced by the spatially resolved surface photovoltage spectroscopy (SRSPS) analysis[35] on the single particle of Ir/BVO-573 and Ir(P.I.)/BVO-573. First of all, the contact potential difference (CPD) values on both {010} and {110} facets of both particles under photoirradiation and dark were measured with results given in Figure S8, based on which the SPV value (i.e., difference of CPD under irradiation and dark) on the Ir(P.I.)/BVO-573 particle are generally higher than those of Ir/BVO-573 one (Figure 3A and B), well demonstrating the better promotion effect of photoinduced dual cocatalysts on the charge separation of BVO. Secondly, the promotion extent of photoinduced dual cocatalysts can be quantitatively described by measuring the CPD values obtained along the line direction scanning of both particles (Figure S9). On the basis, the difference of the CPD (ΔCPD, i.e., SPV) on them are calculated and given in Figure 3C and D, respectively. It is found that the ΔSPV value between {110} and {010} facets on the Ir(P.I.)/BVO-573 particle (ca. 97 mV) is over 7-fold higher than that (ca. 13 mV) on the Ir/BVO-573 one (Figure 3C and D). Thirdly, the promotion effect of photoinduced dual cocatalysts on the charge separation can be further supported by results of the steady-state photoluminescence (PL) spectra (Figure S10).

Strikingly, the promotion effect of the loaded dual cocatalysts on the charge separation of the Ir(P.I.)/BVO-n samples is also found to strongly depend on the SMSI interface between the Ir cocatalysts and BVO. By comparing the surface voltage change on the typical powder samples under irradiation and dark, we can find that the SPV amplitude on the Ir(P.I.)/BVO-473 sample is similar to that on the Ir/BVO-PD photocatalyst free of the SMSI effect (Figure S11), implying that here promotion of the charge separation on them mainly results from the effect of photoinduced Ir and IrO_2 cocatalysts. Compared to the Ir(P.I.)/BVO-473, however, the Ir(P.I.)/BVO-673 with worse iridium dispersion but SMSI effect (Figure S2 and Figure 1C) exhibits much higher SPV amplitude (Figure 3E), as confirms that the interfacial SMSI makes an obvious promotion effect on the charge separation of BVO beyond the cocatalysts. Generally, the aggregated dispersion of Ir nanoparticles on the Ir/BVO-673 will not provide abundant interface contact area to cause enough efficient interface charge separation. In this case, the promotion of charge separation can be further enlarged on the Ir(P.I.)/BVO-573 sample with relatively good iridium dispersion and SMSI effect (Figure 3E). It reveals that the interface charge separation is greatly affected by the SMSI and dispersion of cocatalysts.

Similar dependance on the photoinduced cocatalysts and SMSI is also observed for the photocatalytic water oxidation activities. As expected, the obvious photoinduction periods of about 1 h are all observed for the water oxidation on the Ir/BVO-n photocatalysts in the presence of redox $[Fe(CN)_6]^{3-}$ ions (Figure S12), after which the O_2 evolution rates on them become constant and enlarged. This well reveals the importance of photoinduced process to render the metallic Ir and IrO_2 rightly loaded on the {001} and {110} facets of BVO. As seen in Figure 3F, compared with the

Ir(P.I.)/BVO-473 photocatalyst free of SMSI, the constant O_2 evolution rate on the Ir(P.I.)/BVO-673 with worse iridium dispersion is much larger, demonstrating the obvious promotion of SMSI on the water oxidation. Compared with the pristine BVO photocatalyst, furthermore, the increase of O_2 evolution rate on the Ir(P.I.)/BVO-573 photocatalyst (150 μmol/h) is much larger than the summation of increase on the Ir(P.I.)/BVO-673 (56 μmol/h) and Ir(P.I.)/BVO-473 (40 μmol/h) sample, further revealing the importance of SMSI as well as dispersion of cocatalysts.

Photocatalytic performance of Z-scheme OWS

The photoinduced Ir(P.I.)/BVO-573 sample was finally employed as the OEP to construct Z-scheme OWS together with the ZrO_2-modified TaON (denoted as ZrO_2/TaON) or $MgTa_2O_{6-x}N_y$/TaON heterostructure as the HEP and $[Fe(CN)_6]^{3-/4-}$ as redox ions in a suspended solution. The HEPs were similarly synthesized according to our previous report[29] with preparative details given in the experimental section, whose results of basic structural characterizations are shown in Figure S13 and Figure S14. Figure 4A and Figure S15 give their typical time course of photocatalytic Z-scheme OWS, in which the H_2 and O_2 are evolved with molar ratio of 2:1 at the experimental region. Regardless of using $Rh_yCr_{2-y}O_3$-ZrO_2/TaON or $Rh_yCr_{2-y}O_3$-$MgTa_2O_{6-x}N_y$/TaON as the HEP, the rates of H_2 and O_2 evolution can similarly reach ca. 200 and 100 μmol/h, respectively. The multiple-cycle of time-course curves under visible light and AM 1.5G solar simulator are given in Figure 4B and Figure S16, which show no obvious decay in the experimental region, demonstrating its good photochemical stability. The wavelength-dependent trend of the AQE value during OWS (Figure 4C) is in good accordance with the UV-Vis diffuse reflectance spectra (DRS) of the OEP and HEP, indicating that the Z-scheme OWS system is driven by visible light excitation. The optimal AQE at 420 ± 10 nm was evaluated as 16.9%, and the corresponding STH energy conversion efficiency was calculated as 0.8% (Figure S16 and Table S2). To our knowledge, this should be the first report that the metal-support interaction can be successfully used for significant promotion on the photocatalytic OWS performance. Moreover, both the AQE and STH values reported here should be the highest among the suspended particulate photocatalytic Z-scheme OWS systems under visible light irradiation (Figure 4D). The solar energy conversion efficiency is also comparable to the natural photosynthesis in most plants, whose efficiencies are generally located in the region of 0.1%~1%[36]. It is worthy of being mentioned that the STH value reported here is also superior to the recently reported $SrTiO_3$:Al with a quantum efficiency of almost unity under UV light (STH: 0.76%)[37] and visible-light-responsive InGaN/GaN (STH: 0.5%) at room temperature[38].

DISCUSSION

Here, we give the first demonstration that the existence of SMSI could obviously promote the interfacial charge separation as well as photocatalytic OWS activity of one supported metal photocatalyst. Together with the photoinduction treatment to render the deposited iridium to be controllably converted into the metallic Ir and IrO_2 on the corresponding {010} and {110} facets of BVO, the charge separation as well as water oxidation activity on the Ir(P.I.)/BVO-573 could be significantly promoted. On the basis of it, we finally fabricate one photocatalytic OWS system with benchmarking STH efficiency of artificial photosynthesis using suspended powder photocatalyst. The promotion effect of metal-support interaction on the charge separation as well as photocatalytic OWS performance discovered in this work should open a new venue of constructing efficient supported metal photocatalysts for promising energy and environmental photocatalysis.

EXPERIMENTAL PROCEDURES

Resource Availability

Lead Contact

Further information and requests for resources should be directed to and will be fulfilled by the Lead Contact, Fuxiang Zhang (fxzhang@dicp.ac.cn).

Materials Availability

This study did not generate new unique reagents.

Data and Code Availability

The data generated during this study are available in the main text and the supplemental information.

Synthesis of HEPs

ZrO_2/TaON (Zr/Ta = 0.1) and $MgTa_2O_{6-x}N_y$/TaON (Mg/Ta = 0.15) were synthesized by nitridation of the ZrO_2/Ta_2O_5 and $MgTa_2O_6/Ta_2O_5$ composite, respectively under an ammonia flow (20 mL min^{-1}) at 1123 K for 15 h by referring to the previous works[28,39].

The deposition of nanoparticulate rhodium-chromium mixed oxides (denoted as $Rh_yCr_{2-y}O_3$) as the cocatalyst was carried out by the photodeposition method. 0.2 g

ZrO_2/TaON (or $MgTa_2O_{6-x}N_y$/TaON) was dispersed in 150 mL solution containing 20 *vol*% methanol. A certain amount of Na_3RhCl_6 and K_2CrO_4 (1.0 *wt*% Rh and 1.5 *wt*% Cr for ZrO_2/TaON, 2.5 *wt*% Rh and 3.75 *wt*% Cr for $MgTa_2O_{6-x}N_y$/TaON) were also added to provide the precursor. The deposition was performed under the full-spectrum irradiation for 6 h. Whereafter, the solution was centrifuged and washed with distilled water for three times, and then dried at 353 K for overnight to get the HEPs (denoted as $Rh_yCr_{2-y}O_3$-ZrO_2/TaON and $Rh_yCr_{2-y}O_3$-$MgTa_2O_{6-x}N_y$/TaON, respectively).

Preparation of BVO-based samples

1) Synthesis of BVO

Typically, 10 mmol NH_4VO_3 was first diffused in 50 mL distilled water, into which about 8 mL nitric acid was added to fully dissolve NH_4VO_3 with stirring. Afterwards, $Bi(NO_3)_3 \cdot 5H_2O$ (10 mmol) was added with stirring kept for about 30 mins. Secondly, the ammonia solution (25-28 *wt*%) was added drop by drop into the mixture until the pH value was adjusted to be about 0.5. After another 2 h stirring, the mixed solution was transferred to a Teflon-lined stainless steel autoclave for hydrothermal treatment at 473 K for 10 h. Finally, the cooled solution was filtrated, fully washed with distilled water and dried for use.

2) Preparation of Ir/BVO-n and Ir(P.I.)/BVO-n samples

0.2 g BVO was immersed in a calculated K_2IrCl_6 (0.8 *wt*%, the concentration of solution: 1 mg mL^{-1}) aqueous solution with ultrasonic agitation for ca. 5 min. After the solution was completely evaporated in a water bath at 353 K, it was reduced at 473 K, 573 K, 673 K for 1 h under a flow of 5% H_2/Ar (200 mL min^{-1}), respectively. And the obtained samples were correspondingly named as Ir/BVO-473, Ir/BVO-573 and Ir/BVO-673. Furthermore, all above samples are photoinduced under the presence of $[Fe(CN)_6]^{3-}$ to rationally convert the deposited iridium species into metallic Ir on the {010} and IrO_2 on the {110} facets, respectively. The corresponding samples are denoted as Ir(P.I.)/BVO-n, where n stands for the reduction temperature.

3) Preparation of Ir/BVO-PD sample

0.2 g BVO powder was dispersed in deionized water containing a calculated amount of Na_3IrCl_6 (0.8 *wt*%, the concentration of solution: 1 mg mL^{-1}). The well mixed solution was then irradiated by 300 W xenon lamp without cut-off filter for 2 h.

Photocatalytic reactions

All the tests of photocatalytic activities were carried out in a Pyrex top irradiation-type reaction vessel, which was connected to a closed gas circulation system to evacuate the reaction system containing suspended solution of powder photocatalysts. The mixed suspended solution with temperature of 288 K maintained by a flow of cooling water was irradiated using a 300 W Xenon lamp with a cut-off filter (Hoya, L-42; $\lambda \geq 420$ nm). The gases evolved were analyzed by gas chromatography (Agilent; GC-7890A, MS-5A column, TCD, Ar carrier). During the photocatalytic water oxidation, 50 mg Ir/BVO-n was dispersed in the 100 mL 25 mM sodium phosphate buffer solution (pH = 6.0) containing $K_3[Fe(CN)_6]$ (5 mM). As for the photocatalytic Z-scheme overall water splitting (OWS), 35 mg Ir(P.I.)/BVO-573 and 100 mg $Rh_yCr_{2-y}O_3$-ZrO_2/TaON (or 150 mg $Rh_yCr_{2-y}O_3$-$MgTa_2O_{6-x}N_y$/TaON) were dispersed in the 100 mL 25 mM sodium phosphate buffer solution (pH = 6.0) containing $K_4[Fe(CN)_6]$ (10 mM).

Measurements of AQE and STH conversion efficiency

The AQE was measured using a 300 W xenon lamp equipped with band-pass filters (Asahi Spectra Co., FWHM: 10 nm) through a Pyrex top-irradiation-type reaction vessel. The incident number of photons was measured using a calibrated Si photodiode (LS-100, EKO Instruments Co., LTD.), and the equation of AQE (φ) is as follows:

$$\varphi(\%) = (AR/I) \times 100 \qquad (1)$$

where *A*, *R*, and *I* are coefficients. The A is a coefficient (4 for H_2 evolution; 8 for O_2 evolution) and R is the evolution rate of H_2 or O_2. After testing, the total number of photons at 420, 460, 480, 500, and 560 nm reaching the reaction solution are measured to be 8.4×10^{20}, 6.5×10^{20}, 7.1×10^{20}, 4.8×10^{20}, and 6.9×10^{20} photons h^{-1}, respectively. The reaction condition is that 50 mg Ir(P.I.)/BVO-573 and 150 mg ZrO_2/TaON were dispersed in the 150 mL 25 mM sodium phosphate buffer solution (pH = 6.0) containing $K_4[Fe(CN)_6]$ (10 mM). And the cooling water was used to maintain the reaction system at 298 K. The evolution rates of H_2 under the wavelength of 420, 460, 480, 500, and 560 nm were tested to be 58.6, 31.2, 24.1, 10.5 and 0 μmol h^{-1}, respectively.

The equation of STH energy conversion efficiency (η) is as follows:

$$\eta(\%) = (R_H \times \Delta G^{\theta})/(P \times S) \times 100 \qquad (2)$$

The R_H represents the rate of H_2 evolution (mol s^{-1}). The ΔG^{θ} denotes the standard Gibbs energy of water (237.13×10^3 J mol^{-1}). The *P* is the intensity of simulated sunlight (0.1 W cm^{-2}) and *S* is the irradiation area (4.0 cm^2). The light source is an AM

1.5G solar simulator (XES-40S2-CE, San-Ei Electric) through the top-irradiation reaction vessel. The reaction condition is that 50 mg Ir(P.I.)/BVO-573 and 150 mg ZrO_2/TaON were dispersed in the 150 mL 25 mM sodium phosphate buffer solution (pH = 6.0) containing $K_4[Fe(CN)_6]$ (10 mM). And the cooling water was used to maintain the reaction system at 288 K. The initial rates of H_2 and O_2 evolution are about 48 and 24 μmol/h, separately.

SUPPLEMENTAL INFORMATION

Supplemental information can be found online at XXX.

ACKNOWLEDGMENTS

This work was financially supported by the National Natural Science Foundation of China (22332005, 22279138, 21925206), the National Key R&D Program of China (2020YFA0406102). We would like to thank Z. Ren from Dalian Institute Chemical Physics, Chinese Academy of Sciences for his discussion on the XPEEM data.

AUTHOR CONTRIBUTIONS

F.Z. conceived and designed the experiments, and revised the manuscript. Y.Q. performed most of the synthetic work, activity test, catalyst characterizations, and wrote the draft. B.Z. and G.M. carried out the SRSPS measurements and analysis. G.Z. conducted XPEEM measurement with data analysis. Z.Z. performed the PL measurements. T.X. conducted the SPV characterizations. S.C. assisted the synthesis of $MgTa_2O_{6-x}N_y$/TaON heterostructure photocatalyst. Both C.L. and K.D. revised the manuscript with constructive comments. K.D. instructed the synthesis of HEPs. All authors discussed the results and contributed to the manuscript.

DECLARATION OF INTERESTS

K.D. is an advisory board member of this journal.

REFERENCES

1. Tauster, S., J. Fung, S. C., and Garten, R. L. (1978). Strong metal-support interactions. group 8 noble metals supported on TiO_2. J. Am. Chem. Soc. *100*, 170–175. 10.1021/ja00469a029.
2. Fu, Q., and Wagner, T. (2007). Interaction of nanostructured metal overlayers with oxide surfaces. Surf. Sci. Rep. *62*, 431–498. 10.1016/j.surfrep.2007.07.001.
3. van Deelen, T. W., Mejía, C. H., and de Jong K. P. (2019). Control of metal-support interactions in heterogeneous catalysts to enhance activity and selectivity. Nat. Catal. *2*, 955–970. 10.1038/s41929-019-0364-x.
4. Lou, Y., Xu, J., Zhang, Y., Pan, C., Dong, Y., and Zhu, Y. (2020). Metal-support interaction for heterogeneous catalysis: from nanoparticles to single atoms. Mater. Today Nano *12*, 100093. 10.1016/j.mtnano.2020.100093.
5. Zhang, L., Zhou, M., Wang, A., and Zhang, T. (2020). Selective hydrogenation over supported metal catalysts: from nanoparticles to single atoms. Chem. Rev. *120*, 683–733. 10.1021/acs.chemrev.9b00230.
6. Ro, I., Resasco, J., and Christopher, P. (2018). Approaches for understanding and

controlling interfacial effects in oxide-supported metal catalysts. ACS Catal. *8*, 7368–7387. 10.1021/acscatal.8b02071.

7. Willinger, M. G., Zhang, W., Bondarchuk, O., Shaikhutdinov, S., Freund, H.-J., and Schlögl, R. (2014). A case of strong metal-support interactions: combining advanced microscopy and model systems to elucidate the atomic structure of interfaces. Angew. Chem. Int. Ed. *53*, 5998–6001. 10.1002/anie.201400290.
8. Bruix, A., Rodriguez, J. A., Ramírez, P. J., Senanayake, S. D., Evans, J., Park, J. B., Stacchiola, D., Liu, P., Hrbek, J., and Francesc I. (2012). A new type of strong metal-support interaction and the production of H_2 through the transformation of water on Pt/CeO_2(111) and Pt/CeO_x/TiO_2(110) catalysts. J. Am. Chem. Soc. *134*, 8986–8974. 10.1021/ja302070k.
9. Liu, X., Liu, M.-H., Luo, Y.-C., Mou, C.-Y., Lin, S. D., Cheng, H., Chen, J.-M., Lee, J.-F., and Lin, T.-S. (2012). Strong metal-support interactions between gold nanoparticles and ZnO nanorods in CO oxidation. J. Am. Chem. Soc. *134*, 10251–10258. 10.1021/ja3033235.
10. Dong, J., Fu, Q., Jiang, Z., Mei, B., and Bao, X. (2018). Carbide-supported Au catalysts for water-gas shift reactions: a new territory for the strong metal-support interaction effect. J. Am. Chem. Soc. *140*, 13808–13816. 10.1021/jacs.8b08246.
11. Li, H., Wang, L., Dai, Y., Pu, Z., Lao, Z., Chen, Y., Wang, M., Zheng, X., Zhu, J., Zhang, W., et al., (2018). Synergetic interaction between neighbouring platinum monomers in CO_2 hydrogenation. Nature Nanotech. *13*, 411–417. 10.1038/s41565-018-0089-z.

12. Gerber, I. C., and Serp, P. A. (2020). Theory/experience description of support effects in carbon-supported. Chem. Rev. *120*, 1250–1349. 10.1021/acs.chemrev.9b00209.

13. Motagamwala, A. H., Almallahi, R., Wortman, J., Igenegbai, V. O., and Linic, S. (2021). Stable and selective catalysts for propane dehydrogenation operating at thermodynamic limit. Science *373*, 217–222. 10.1126/science.abg7894.

14. Zhang, X., Zhang, M., Deng, Y., Xu, M., Artiglia, L., Wen, W., Gao, R., Chen, B., Yao, S., Zhang, X., et al., (2021). A stable low-temperature H_2-production catalyst by crowding Pt on α-MoC. Nature *589*, 396–401. 10.1038/s41586-020-03130-6.

15. Kudo, A., and Miseki, Y. (2009). Heterogeneous photocatalyst materials for water splitting. Chem. Soc. Rev. *38*, 253–278. 10.1039/b800489g.

16. Ismail, A. A., and Bahnemann, D. F. (2014). Photochemical splitting of water for hydrogen production by photocatalysis: A review. Sol. Energy Mater. Sol. Cells. *128*, 85–101. 10.1016/j.solmat.2014.04.037.

17. Kim, D., Sakimoto, K. K., Hong, D., and Yang, P. (2015). Artificial photosynthesis for sustainable fuel and chemical production. Angew. Chem. Int. Ed. *54*, 3259–3266. 10.1002/anie.201409116.

18. Chen, S., Qi, Y., Li, C., Domen, K., and Zhang, F. (2018). Surface strategies for particulate photocatalysts toward artificial photosynthesis. Joule *2*, 2260–2288. 10.1016/j.joule.2018.07.030.

19. Wang, Q., and Domen, K. (2020). Particulate photocatalysts for light-driven water splitting: mechanisms, challenges, and design strategies. Chem. Rev. *120*, 919–

985. 10.1021/acs.chemrev.9b00201.

20. Navalón, S., Dhakshinamoorthy, A., Álvaro, M., Ferrer, B., and García, H.(2023). Metal−organic frameworks as photocatalysts for solar-driven overall water splitting. Chem. Rev. *123*, 445−490. 10.1021/acs.chemrev.2c00460.

21. Yang, J., Wang, D., Han, H., and Li, C. (2013). Roles of cocatalysts in photocatalysis and photoelectrocatalysis. Acc. Chem. Res. *46*, 1900–1909. 10.1021/ar300227e.

22. Zong, X., Yan, H., Wu, G., Ma, G., Wen, F., Wang, L., and Li, C. (2008). Enhancement of photocatalytic H_2 evolution on CdS by loading MoS_2 as cocatalyst under visible light irradiation. J. Am. Chem. Soc. *130*, 7176–7177. 10.1021/ja8007825.

23. Zhang, F., Yamakata, A., Maeda, K., Moriya, Y., Takata, T., Kubota, J., Teshima, K., Oishi, S., and Domen, K. (2012). Cobalt-modified porous single-crystalline $LaTiO_2N$ for highly efficient water oxidation under visible light. J. Am. Chem. Soc. *134*, 8348–8351. 10.1021/ja301726c.

24. Kudo, A., Ueda, K., Kato, H., and Mikami, I. (1998). Photocatalytic O_2 evolution under visible light irradiation on $BiVO_4$ in aqueous $AgNO_3$ solution. Catal. Lett. *53*, 229–230. 10.1023/A:1019034728816.

25. Li, R., Zhang, F., Wang, D., Yang, J., Li, M., Zhu, J., Zhou, X., Han, H., and Li, C. (2013). Spatial separation of photogenerated electrons and holes among {010} and {110} crystal facets of $BiVO_4$. Nat. Commun. *4*, 1432. 10.1038/ncomms2401.

26. Suarez, C. M., Hernández, S., and Russo, N. (2015). $BiVO_4$ as photocatalyst for

solar fuels production through water splitting: A short review. Appl. Catal. A Gen. *504*, 158–170. 10.1016/j.apcata.2014.11.044.

27. Jo, W. J., Kang, H. J., Kong, K. J., Lee, Y. S., Park, H., Lee, Y., Buonassisi, T., Gleason, K. K., and Lee, J. S. (2015). Phase transition-induced band edge engineering of $BiVO_4$ to split pure water under visible light. Proc. Natl. Acad. Sci. U.S.A. *112*, 13774–13778. 10.1073/pnas.1509674112.

28. Qi, Y., Zhang, J., Kong, Y., Zhao, Y., Chen, S., Li, D., Liu, W., Chen, Y., Xie, T., Cui, J., et al. (2022). Unraveling of cocatalysts photodeposited selectively on facets of $BiVO_4$ to boost solar water splitting. Nat. Commun. *13*, 484. 10.1038/s41467-022-28146-6.

29. Wang, W., Favaro, M., Chen, E., Trotochaud, L., Bluhm, H., Choi, K. S., van de Krol, R., Starr, D. E., and Galli, G. (2022). Influence of excess charge on water adsorption on the $BiVO_4$ (010) surface. J. Am. Chem. Soc. *144*, 17173–17185. 10.1021/jacs.2c07501.

30. Li, C., Fan, W., Chen, S., and Zhang, F. (2022). Effective charge carrier utilization of $BiVO_4$ for solar overall water splitting. Chem. Eur. J. *28*, e202201812. 10.1002/chem.202201812.

31. Li, R., Han, H., Zhang, F., Wang, D., and Li, C. (2014). Highly efficient photocatalysts constructed by rational assembly of dual-cocatalysts separately on different facets of $BiVO_4$. Energy Environ. Sci. *7*, 1369–1376. 10.1039/c3ee43304h.

32. Meekins, B. H., and Kamat, P. V. (2011). Role of water oxidation catalyst IrO_2 in

shuttling photogenerated holes across TiO_2 interface. J. Phys. Chem. Lett. *2*, 2304–2310. 10.1021/jz200852m.

33. Frame, F. A., Townsend, T. K., Chamousis, R. L., Sabio, E. M., Dittrich, T., Browning, N. D., and Osterloh, F. E. (2011). Photocatalytic water oxidation with nonsensitized IrO_2 nanocrystals under visible and UV light. J. Am. Chem. Soc. *133*, 7264–7267. 10.1021/ja200144w.

34. Freakley, S. J. Ruiz-Esquius, J. D., and Morgan, J. (2017). The X-ray photoelectron spectra of Ir, IrO_2 and $IrCl_3$ revisited. Surf. Interface Anal. *49*, 794–799. 10.1002/sia.6225.

35. Zhu, J., Fan, F., Chen, R., An, H., Feng, Z., and Li, C. (2015). Direct imaging of highly anisotropic photogenerated charge separations on different facets of a single $BiVO_4$ photocatalyst. Angew. Chem. Int. Ed. *54*, 9111–9242. 10.1002/anie.201504135.

36. Dogutan, D. K., and Nocera, D. G. (2019). Artificial photosynthesis at efficiencies greatly exceeding that of natural photosynthesis. Acc. Chem. Res. *52*, 3143–3148. 10.1021/acs.accounts.9b00380.

37. Nishiyama, H., Yamada, T., Nakabayashi, M., Maehara, Y., Yamaguchi, M., Kuromiya, Y., Nagatsuma, Y., Tokudome, H., Akiyama, S., Watanabe, T., et al., (2021). Photocatalytic solar hydrogen production from water on a 100-m^2 scale. Nature *598*, 304–307. 10.1038/s41586-021-03907-3.

38. Zhou, P., Navid, I. A., Ma, Y., Xiao, Y., Wang, P., Ye, Z., Zhou, B., Sun, K., and Mi, Z. (2023). Solar-to-hydrogen efficiency of more than 9% in photocatalytic water

splitting. Nature *613*, 66–70. 10.1038/s41586-022-05399-1.

39. Maeda, K., Higashi, M., Lu, D., Abe, R., and Domen, K. (2010). Efficient nonsacrificial water splitting through two-step photoexcitation by visible light using a modified oxynitride as a hydrogen evolution photocatalyst. J. Am. Chem. Soc. *132*, 5858–5868. 10.1021/ja1009025.

Figure 1. Identification of SMSI over Ir/BVO photocatalysts

(A) Representative high resolution transmission electron microscopy (HRTEM) image of Ir/BVO-573.

(B) The Ir 4*f* XPS spectra of the Ir/BVO-573, Ir/BVO-673 and Ir/BVO-PD.

(C) Diffuse reflectance infrared Fourier transform spectra of CO obtained after CO adsorption and evacuation with argon at room temperature (inset: the diagram of SMSI formation over Ir/BVO-n samples).

Figure 2. Photo-induced valence change of Ir element

(A) The diagram of redox-driven Z-scheme OWS based on metallic Ir and IrO_2 on the corresponding {010} and {110} facets of BVO.

(B) The diagram of cocatalysts evolution loaded on the BVO with distinct facets after photoinduction.

(C) Ir 4*f* XPS spectra of Ir/BVO-673 and Ir(P.I.)/BVO-673.

(D) Ir 4*f* XPS spectra recorded from the {010} facets of the single Ir/BVO-573 particle in Figure S7B before and after the irradiation of 515 nm laser for 10 mins.

Figure 3. The promotion effect of SMSI and photoinduced dual cocatalysts (Ir and IrO_2) on the charge separation of BVO

(A) Spatial distribution of SPV signals of Ir/BVO-573.

(B) Spatial distribution of SPV signals of Ir(P.I.)/BVO-573.

(C) CPD differences between the CPD values in the dark and under illumination along the line shown and corresponding height cross section profile Ir/BVO-573.

(D) CPD differences between the CPD values in the dark and under illumination along the line shown and corresponding height cross section profile of Ir(P.I.)/BVO-573.

(E) Comparison of SPV values on the series of Ir(P.I)/BVO-n and parent BVO under chopped visible light irradiation.

(F) The rate of O_2 evolution on the Ir(P.I.)/BVO-n and pristine BVO samples.

Figure 4. Photocatalytic activity of Z-scheme OWS

(A) Time course of Z-scheme OWS on the optimized conditions under visible light irradiation.

(B) Multiple cycles of curve of Z-scheme OWS under visible light irradiation.

(C) Dependence curve of AQE value as a function of irradiation wavelength, and UV-Vis DRS of the ZrO_2/TaON and BVO.

(D) Comparison of AQE value in this work and other reported representative redox-based visible-light-driven Z-scheme OWS at 420 nm in the suspended aqueous solution at room temperature.

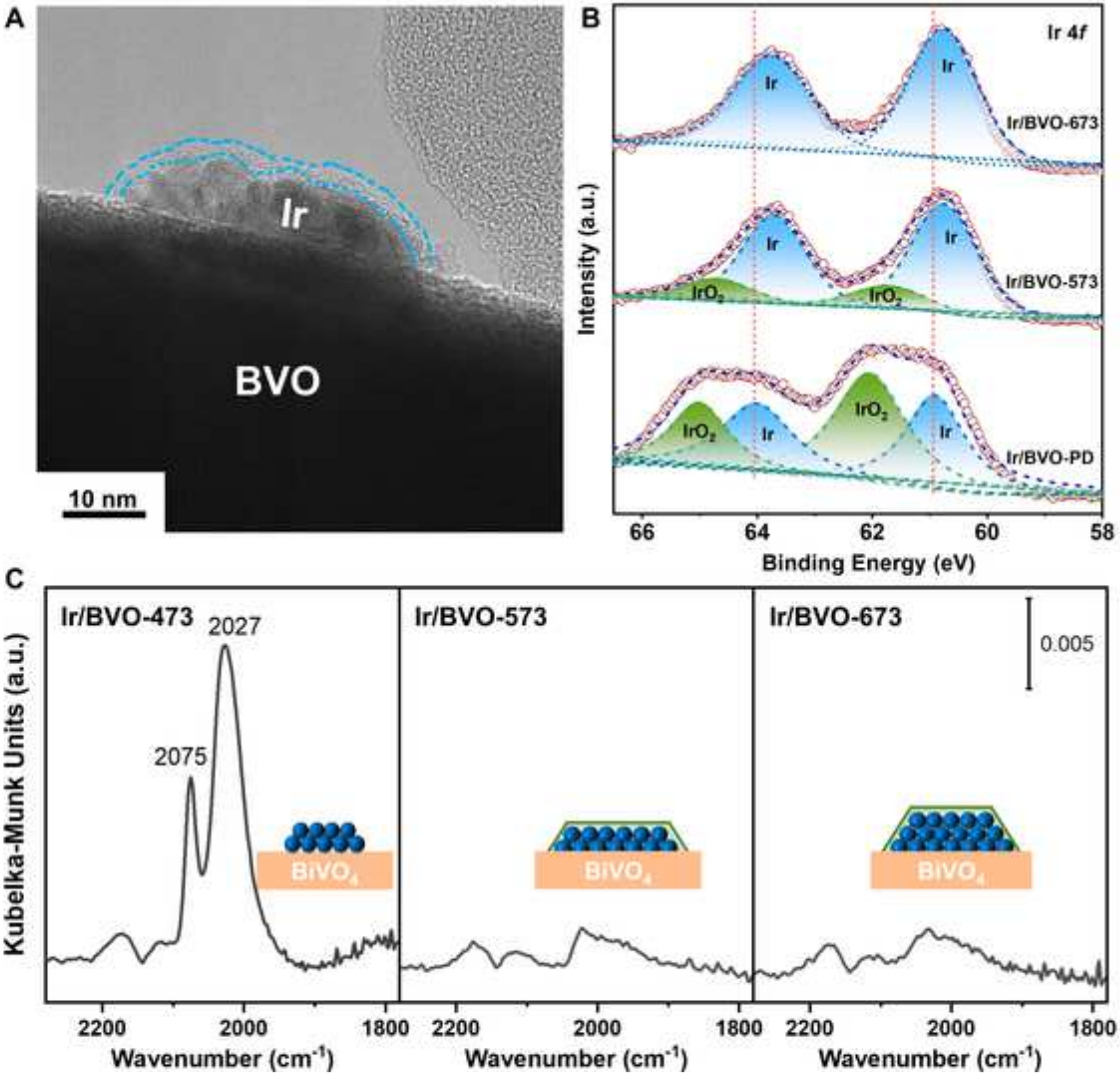
A
Ir
BVO
10 nm
B
Ir 4f
Ir
Ir
Ir/BVO-673
Ir
Ir
IrO$_2$
IrO$_2$
Ir/BVO-573
IrO$_2$
Ir
IrO$_2$
Ir
Ir/BVO-PD
Intensity (a.u.)
66
64
62
60
58
Binding Energy (eV)
C
Kubelka-Munk Units (a.u.)
Ir/BVO-473
2027
2075
BiVO$_4$
Ir/BVO-573
BiVO$_4$
Ir/BVO-673
0.005
BiVO$_4$
2200
2000
1800
Wavenumber (cm^{-1})
2200
2000
1800
Wavenumber (cm^{-1})
2200
2000
1800
Wavenumber (cm^{-1})

Figure 2

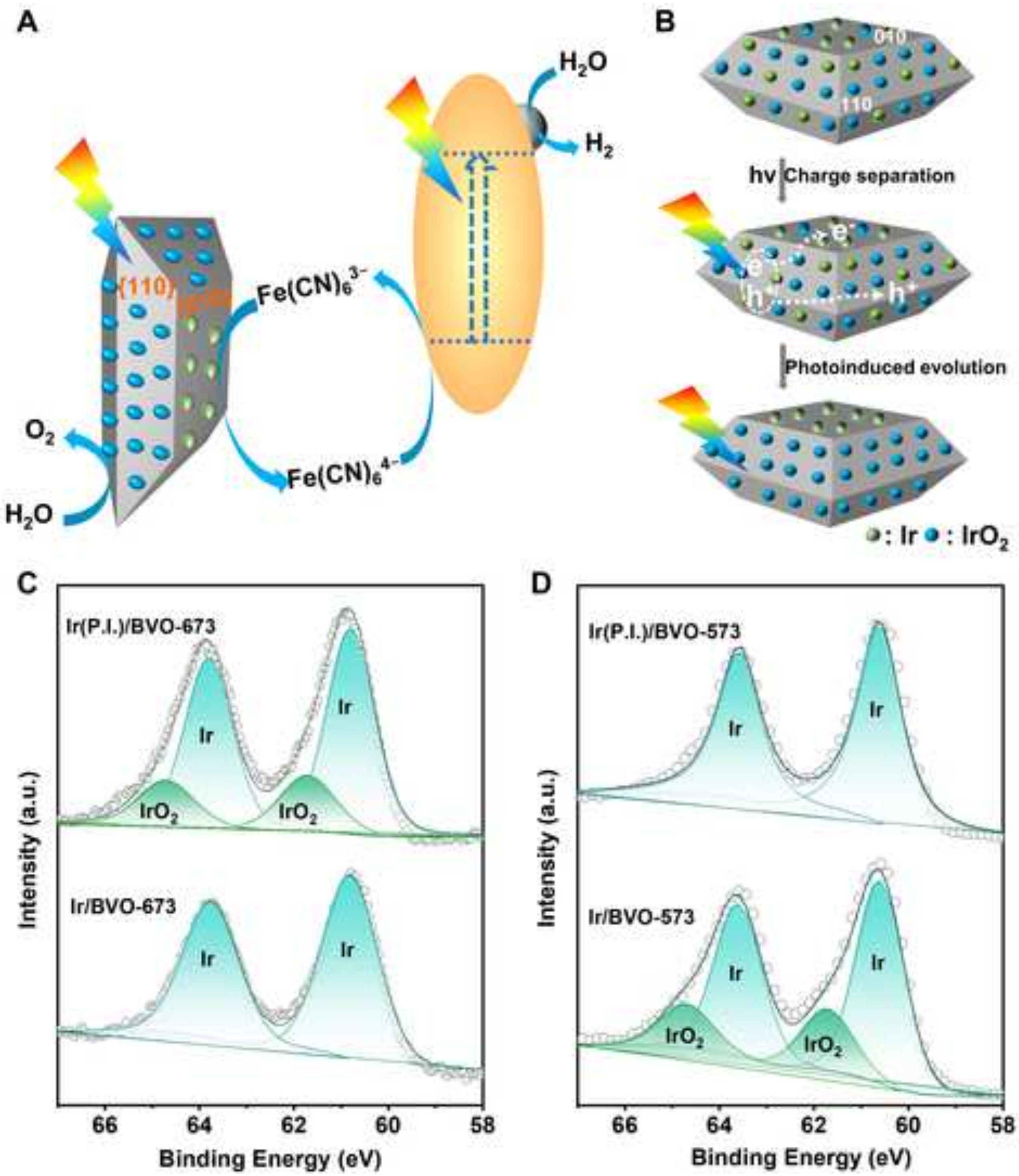
A
{110}
{010}
O_2
H_2O
$Fe(CN)_6^{3-}$
$Fe(CN)_6^{4-}$
H_2O
H_2
B
010
110
hv
Charge separation
e⁻
e⁻
h⁺
h⁺
Photoinduced evolution
: Ir
: IrO_2
C
Ir(P.I.)/BVO-673
Ir
Ir
IrO_2
IrO_2
Ir/BVO-673
Ir
Ir
Intensity (a.u.)
66
64
62
60
58
Binding Energy (eV)
D
Ir(P.I.)/BVO-573
Ir
Ir
Ir/BVO-573
Ir
Ir
IrO_2
IrO_2
Intensity (a.u.)
66
64
62
60
58
Binding Energy (eV)

Figure 3

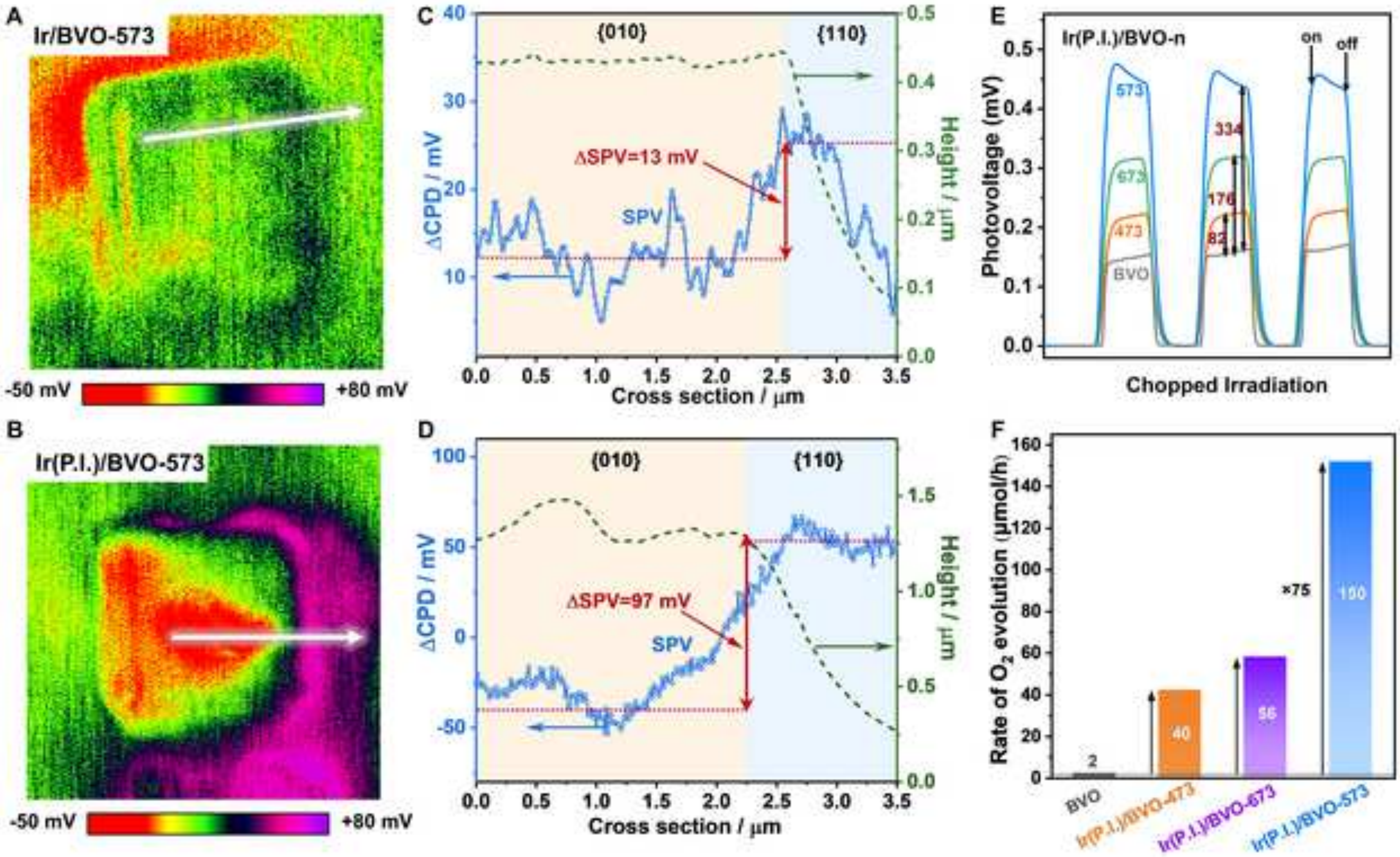
A
Ir/BVO-573
-50 mV
+80 mV
B
Ir(P.I.)/BVO-573
-50 mV
+80 mV
C
{010}
{110}
ΔSPV=13 mV
SPV
ΔCPD / mV
Height / µm
Cross section / µm
D
{010}
{110}
ΔSPV=97 mV
SPV
ΔCPD / mV
Height / µm
Cross section / µm
E
Ir(P.I.)/BVO-n
on
off
573
673
473
BVO
334
176
82
Photovoltage (mV)
Chopped Irradiation
F
Rate of O2 evolution (µmol/h)
2
40
56
150
×75
BVO
Ir(P.I.)/BVO-473
Ir(P.I.)/BVO-673
Ir(P.I.)/BVO-573

Figure 4

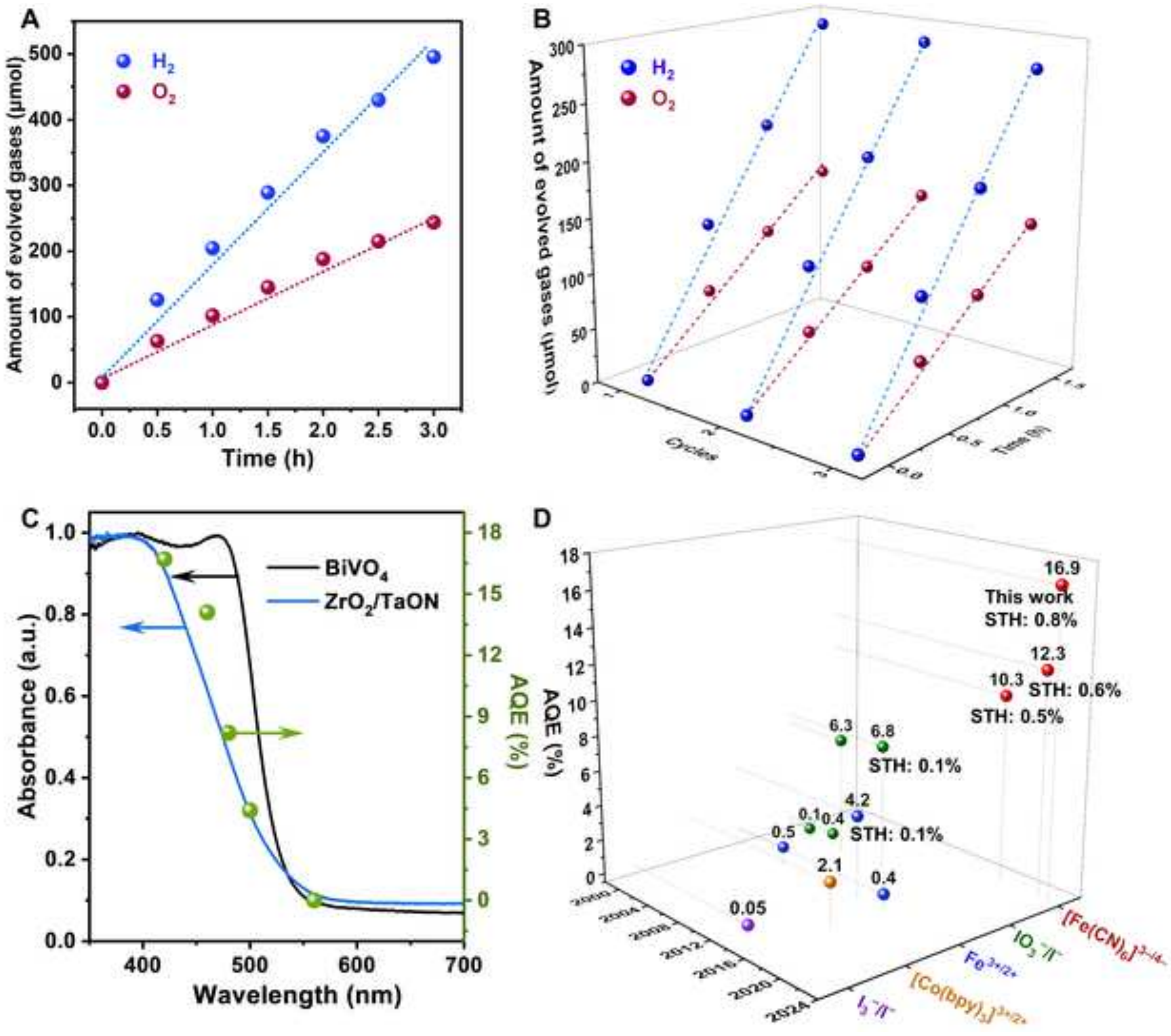
A
Amount of evolved gases (μmol)
0
100
200
300
400
500
Time (h)
0.0
0.5
1.0
1.5
2.0
2.5
3.0
H_2
O_2
B
Amount of evolved gases (μmol)
0
50
100
150
200
250
300
Cycles
1
2
3
Time (h)
0.0
0.5
1.0
1.5
H_2
O_2
C
Absorbance (a.u.)
0.0
0.2
0.4
0.6
0.8
1.0
Wavelength (nm)
400
500
600
700
AQE (%)
0
3
6
9
12
15
18
$BiVO_4$
ZrO_2/TaON
D
AQE (%)
0
2
4
6
8
10
12
14
16
18
2000
2004
2008
2012
2016
2020
2024
I_3^-/I^-
$[Co(bpy)_3]^{3+/2+}$
$Fe^{3+/2+}$
IO_3^-/I^-
$[Fe(CN)_6]^{3-/4-}$
16.9
This work
STH: 0.8%
12.3
STH: 0.6%
10.3
STH: 0.5%
6.3
6.8
STH: 0.1%
4.2
0.1
0.4
STH: 0.1%
0.5
2.1
0.4
0.05

Supplemental Items

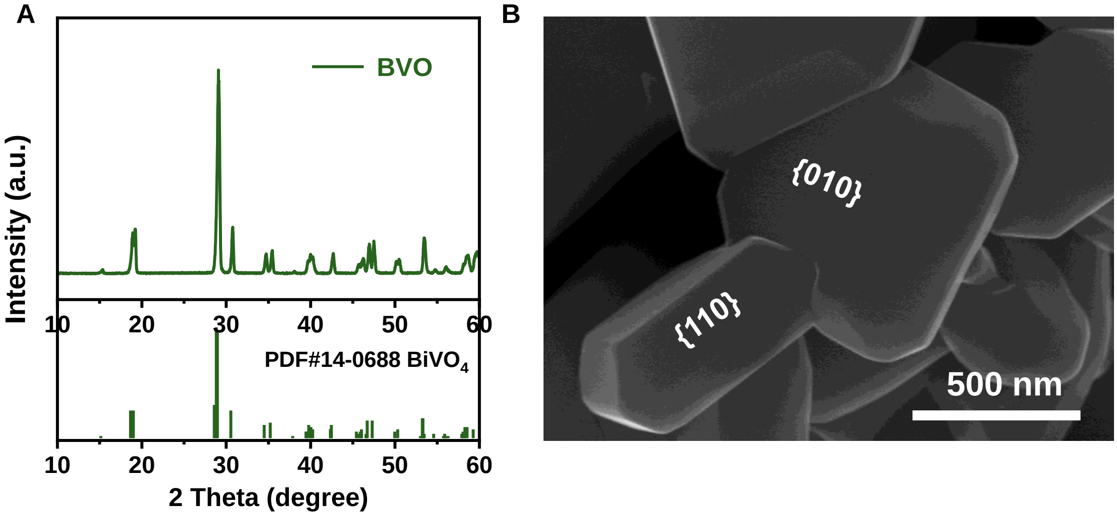

Figure S1. Structural and morphological characteristics of BVO. (A) XRD patterns and (B) FESEM image. According to the XRD patterns, the peaks of obtained sample well match the PDF card of monoclinic phase of BVO. The morphology of BVO prepared through the hydrothermal method is regular decahedron with {010} and {110} facets exposed.

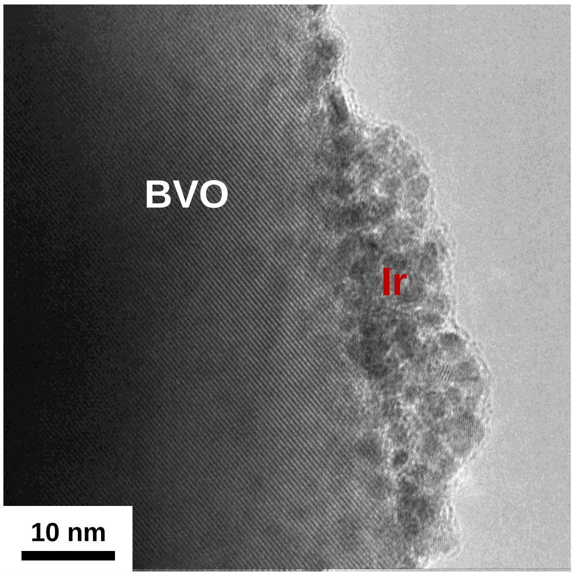

Figure S2. **Typical HRTEM image of Ir/BVO-673 sample.** The Ir nanoparticles loaded on the BVO tend to gather together under the high temperature treatment, but the nanolayer on the surface of Ir nanoparticles can be still observed, indicating the existence of metal-support interaction between Ir and BVO.

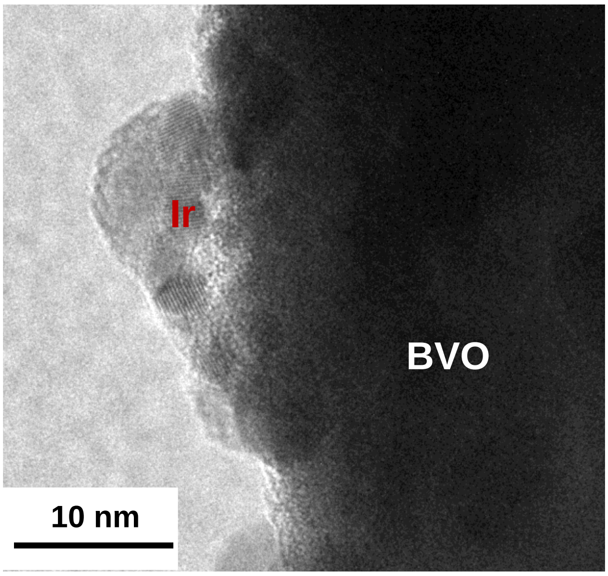

Figure S3. **Typical HRTEM image of Ir/BVO-573 after the O_2/Ar oxidation treatment at 673 K for 30 mins.**

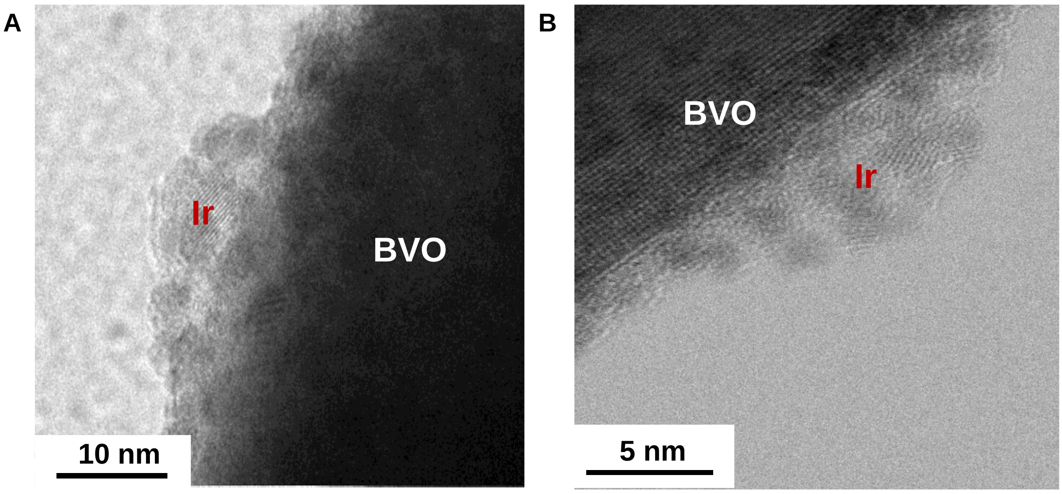

Figure S4. Representative HRTEM images. (A) Ir/BVO-473 and (B) Ir/BVO-PD samples. There is no obvious oxide coverage on the surface of deposited Ir nanoparticles, indicating no metal-support interaction in both Ir/BVO-473 and Ir/BVO-PD sample.

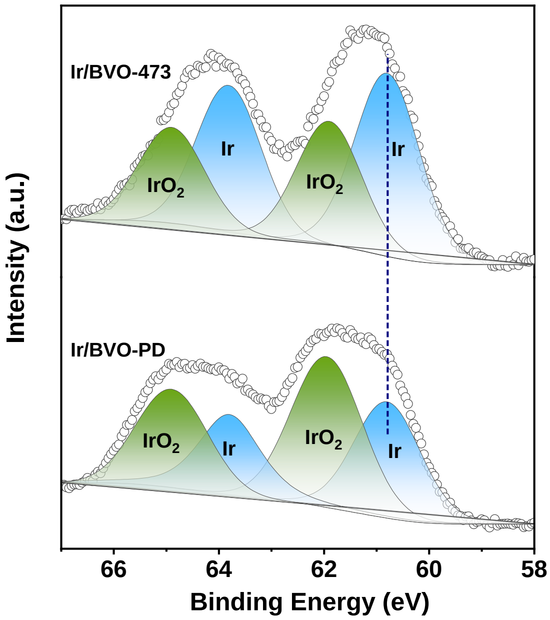

Figure S5. The Ir 4*f* XPS spectra of Ir/BVO-473 and Ir/BVO-PD. The binding energy of Ir^0 on the Ir/BVO-473 is almost the same as that on Ir/BVO-PD sample, indicating their similar interface interaction between Ir and BVO.

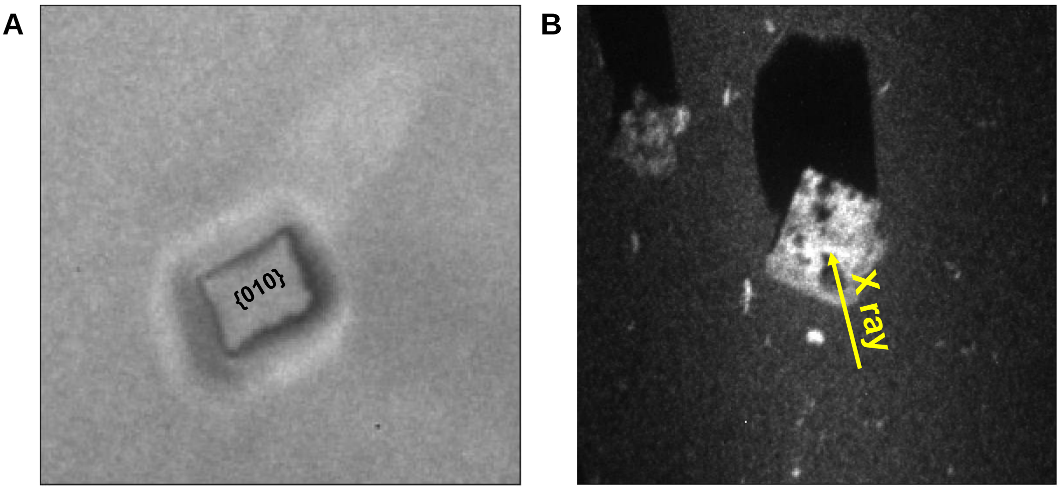

Figure S6. The results of X-ray photoemission electron microscopy (XPEEM) measurement. (A) LEEM image of single Ir/BVO-573 particle recorded at 7 eV and (B) XPEEM image of single Ir/BVO-573 particle with Ir 4*f* photoelectron signals of {010} facets collected and integrated. It should be mentioned that here the shape of individual Ir/BVO-573 particle looks like rectangle from the top view due to the limitation of LEEM resolution (Figure S6A), but the morphology of decanedron can be confirmed by FESEM image (Figure S1B). Affected by the intensity of photoelectron emission and the distribution of Ir elements, the shape of the individual particle also tends to be rectangular under the XPEEM (Figure S6B), where the bright area in the XPEEM image represents the high content of deposited iridium species. On the basis of above morphology observation, we thus could move the particle under the light spots of X-ray and analyze the valence change of iridium species deposited on the {010} facet of BVO under the irradiation of 515 nm laser irradiation. It should be pointed out that both X-ray and 515 nm laser could excite the electrons to cause reduction of IrO_2 into metallic Ir on the {010} facet of BVO, but the direct irradiation of X-ray on the iridium species including IrO_2 does not cause their reduction into metallic Ir. This well rules out the possibility of direct reduction of IrO_2 into Ir by the X-ray.

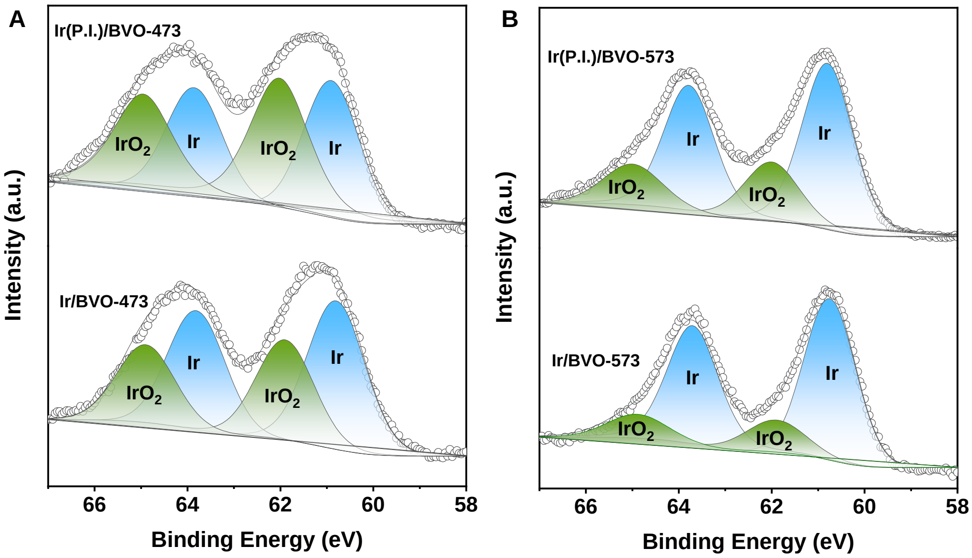

Figure S7. Comparison of the Ir 4*f* XPS spectra before and after the photoinduction. (A) Ir/BVO-473 and Ir(P.I.)/BVO-473. (B) Ir/BVO-573 and Ir(P.I.)/BVO-573. It is found that the contents of IrO_2 species on both Ir(P.I.)/BVO-473 and Ir(P.I.)/BVO-573 sample are increased with respect to their corresponding sample without photoinduction, well demonstrating the existence of photoreduction process of IrO_2 into Ir and photooxidation of Ir into IrO_2 during the photoinduction. We would like to mention again that the photoreduction of deposited IrO_2 species only happens on the {001} facets and the photooxidation of metallic Ir species only proceeds on the {110} facets due to the accumulation of photogenerated electrons and holes on the corresponding {010} and {110} facets of BVO during the irradiation.

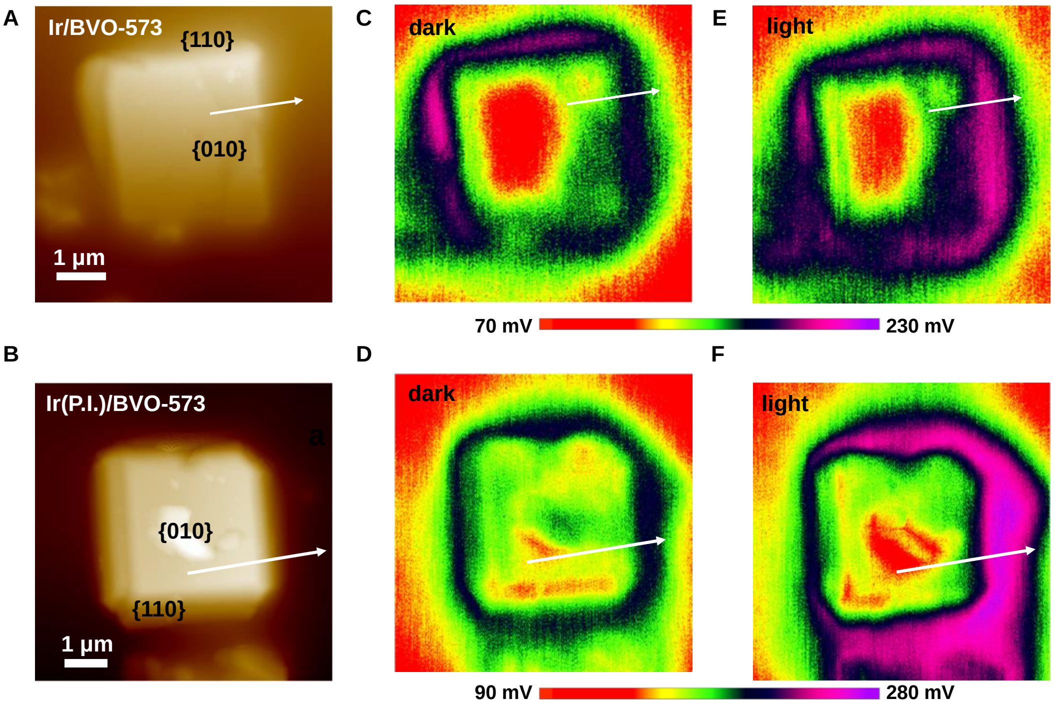

Figure S8. The SRSPS of single particle. Height image of a single particle of Ir/BVO-573 (A) and Ir(P.I.)/BVO-573 (B); Spatially distribution of CPD signals in the dark of Ir/BVO-573 (C) and Ir(P.I.)/BVO-573 (D); Spatially distribution of CPD signals under illumination of Ir/BVO-573 (E) and Ir(P.I.)/BVO-573 (F). The height image shows that the morphology of BVO single particle is decahedron (Figure S8A and B). The CPD values of {110} facet from Ir/BVO-573 and Ir(P.I.)/BVO-573 are both increased under irradiation, indicating the holes accumulation due to the surface band bending. However, the CPD values of {010} facet from Ir/BVO-573 and Ir(P.I.)/BVO-573 is changed in the opposite direction, indicating that the electron accumulation is promoted after photoinduction.

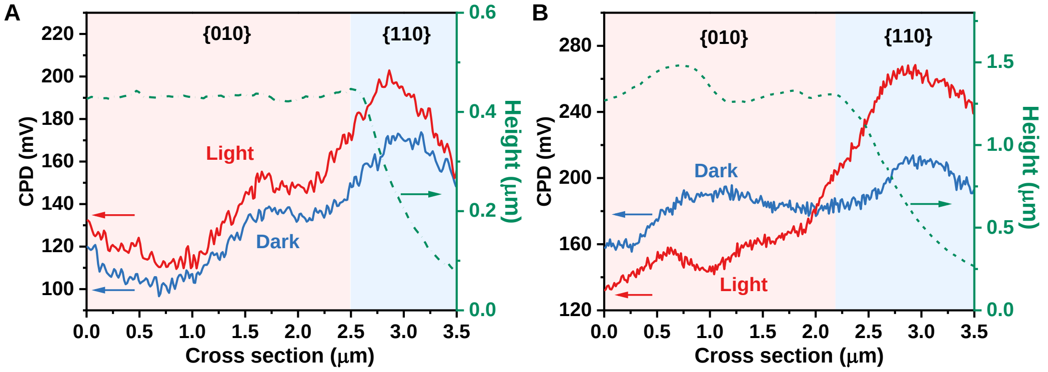

Figure S9. CPD values in the dark and under illumination along the line shown and corresponding height cross section profile. (A) Ir/BVO-573 and (B) Ir(P.I.)/BVO-573.

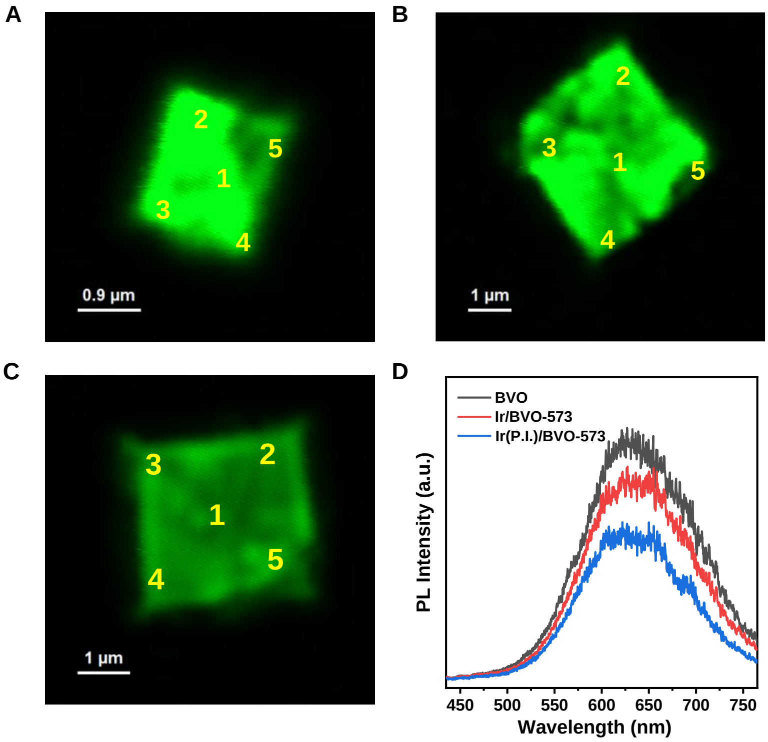

Figure S10. The photoluminescence (PL) images of single particle. (A) BVO, (B) Ir/BVO-573, (C) Ir(P.I.)/BVO-573 and (D) comparison of their average PL intensities collected at five different positions of single BVO, Ir/BVO-573 and Ir(P.I.)/BVO-573 particle. As seen in Figure S10D, the average PL intensity on the Ir(P.I.)/BVO-573 is remarkably lower than that of the BVO or Ir/BVO-573, revealing better promotion of the photoinduced dual cocatalysts on the charge separation of BVO.

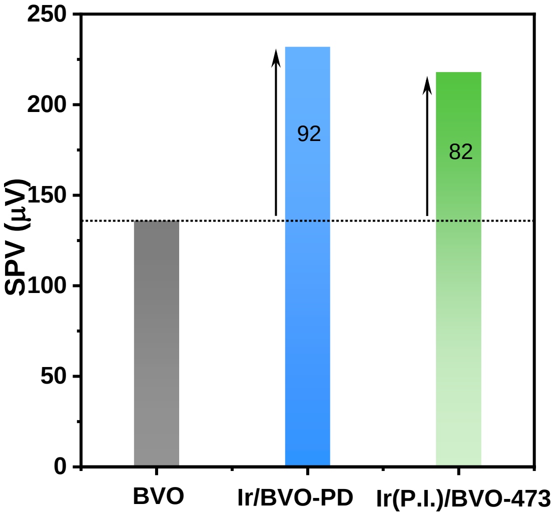

Figure S11. Comparison of SPV values on the BVO, Ir(P.I.)/BVO-473 and Ir/BVO-PD samples obtained under dark and irradiation. As seen in Figure S11, the enhancement of SPV value is observed for both Ir-modified samples with respect to the BVO sample, indicting the promotion effect of deposited iridium on the charge separation. It is worth noting that compared to the pristine BVO, the amplitude increases (ΔSPV) of the SPV signals on the Ir(P.I.)/BVO-473 (ca. 82 μV) is close to that on the Ir(P.D.)/BVO (ca. 92 μV), further implying that the promotion of the charge separation in the Ir(P.I.)/BVO-473 free of SMSI mainly results from the effect of photoinduced iridium cocatalysts.

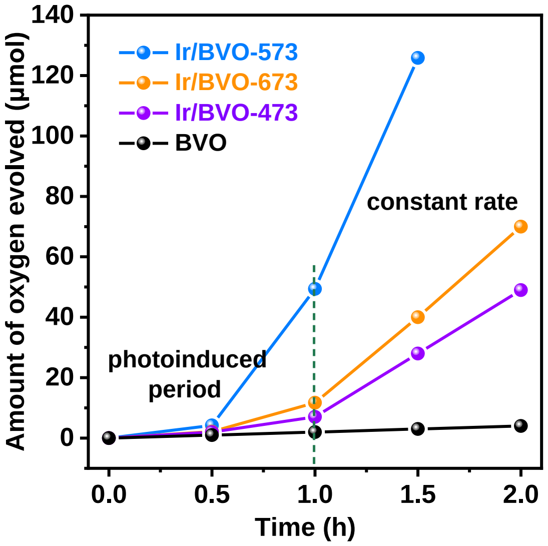

Figure S12. Time courses of O_2 evolution on the series of Ir/BVO-n and pristine BVO samples.

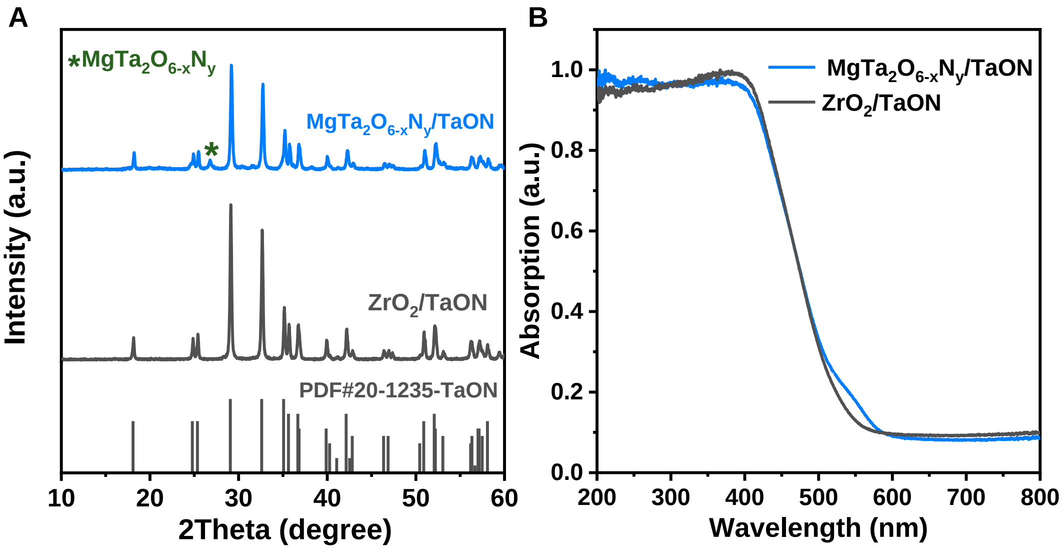

Figure S13. Structural characterizations of $MgTa_2O_{6-x}N_y$/TaON and ZrO_2/TaON. (A) XRD patterns, (B) UV-vis spectra. According to the XRD patterns, the peaks of obtained sample well match the PDF card of pure phase TaON and the peaks marked with asterisk belong to $MgTa_2O_{6-x}N_y$. The absorption of $MgTa_2O_{6-x}N_y$/TaON and ZrO_2/TaON shows wide visible response.

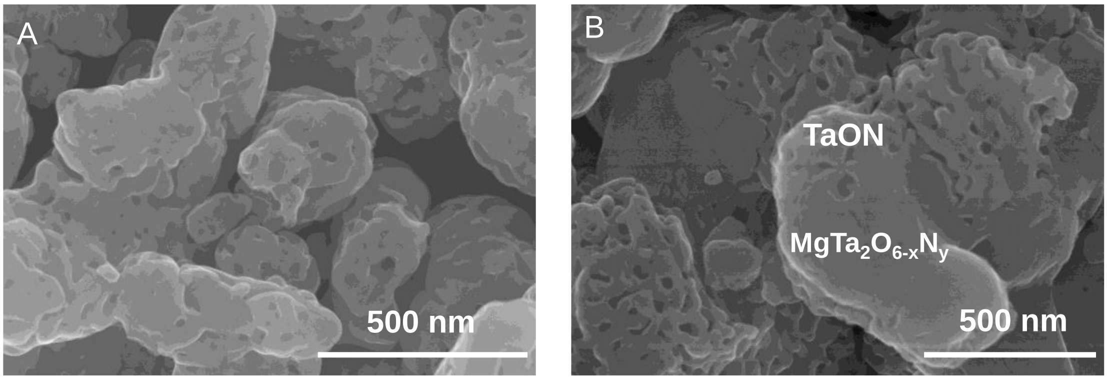

Figure S14. The FESEM images of HEPs. (A) ZrO_2/TaON and (B) $MgTa_2O_{6-x}N_y$/TaON. The surface of TaON is rough and porous (Figure S14A). The heterostructure of $MgTa_2O_{6-x}N_y$/TaON can be observed between the different morphology of $MgTa_2O_{6-x}N_y$ and TaON (Figure S14B).

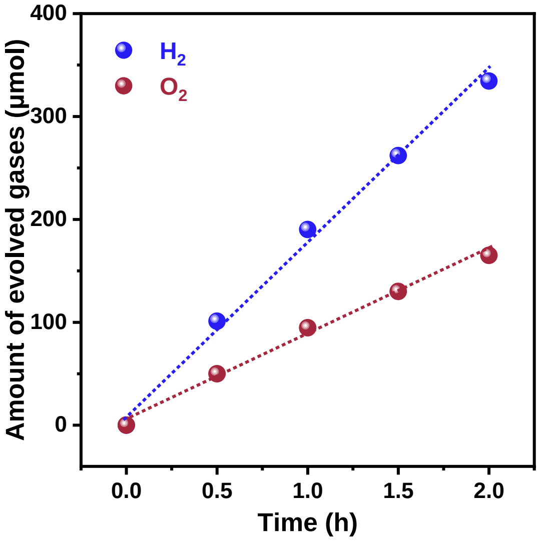

Figure S15. Time courses of photocatalytic Z-scheme OWS under visible light irradiation of Xe lamp. Reaction condition: 35 mg Ir(P.I.)/BVO-573; 150 mg Rh$_y$Cr$_{2-y}$O$_3$-MgTa$_2$O$_{6-x}$N$_y$/TaON; 100 mL 25 mM sodium phosphate buffer solution (pH = 6.0) containing K$_4$[Fe(CN)$_6$] (10 mM).

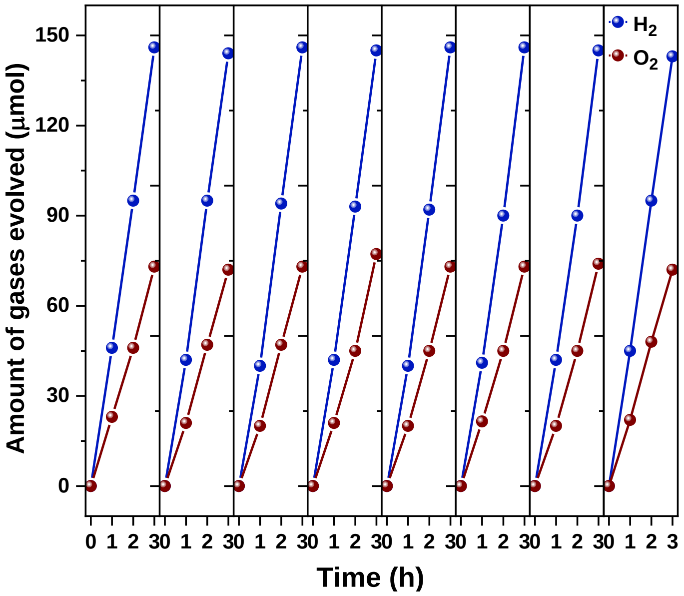

Figure S16. Time courses of photocatalytic Z-scheme OWS under illumination of the standard solar simulator. Reaction condition: 50 mg Ir(P.I.)/BVO-573, 150 mg ZrO_2/TaON, 150 mL 25 mM sodium phosphate buffer solution (pH 6.0) containing $K_4[Fe(CN)_6]$ (10 mM); irradiation area: 4.0 cm^2; temperature: 288 K.

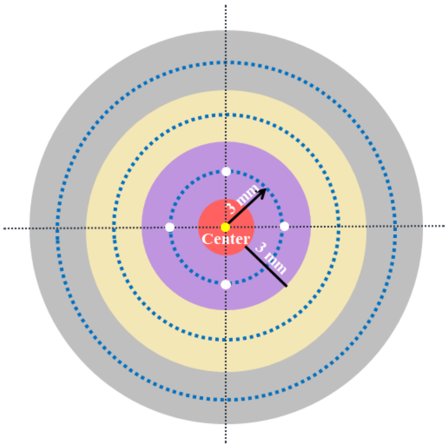

Scheme S1. Schematic diagram of the measurement of the number of incident photons with top-illuminated illumination

Table S1. The relative content of Ir and IrO_2 species on the Ir/BVO-473 and Ir/BVO-573 samples before and after the photoinduction based on X-ray photoelectron spectroscopy (XPS) analysis.

	Ir		IrO_2	
	before	after	Before	after
Ir/BVO-473	56%	46%	44%	54%
Ir/BVO-573	81%	72%	19%	28%

Table S2. Representative redox-based visible-light-driven Z-scheme OWS systems in the suspension system under room temperature.

HEP	OEP	Electron mediator	Light source	Reactant solution	Efficiency	Refs
Dye-adsorbed Pt/$H_4Nb_6O_{17}$	IrO_2-PtO_x/WO_3	I_3^-/I^-	300 W Xe lamp (>420 nm)	pH = 4.5	AQE: 0.05% at 480 nm for H_2 evolution	[1]
Pt/$SrTiO_3$:Rh	$BiVO_4$	$[Co(bpy)_3]^{3+/2+}$ or $[Co(phen)_3]^{3+/2+}$	300 W lamp (>420 nm)	H_2O	AQE: 2.1% at 420 nm	[2]
Pt/$SrTiO_3$:Rh	WO_3	Fe^{3+}/Fe^{2+}	300 W Xe lamp (>420 nm)	pH = 2.4, H_2SO_4 mediated	AQE: 0.5% at 420 nm	[3]
Ru/$SrTiO_3$:Rh	Bi_4NbO_8Cl	Fe^{3+}/Fe^{2+}	300 W Xe lamp (>420 nm)	pH = 2.5, HCl mediated	AQE: 0.4% at 420 nm for O_2 evolution	[4]
Ru/$SrTiO_3$:Rh	$BiVO_4$	Fe^{3+}/Fe^{2+}	300 W Xe lamp (>420 nm)	pH = 2.4, H_2SO_4 mediated	AQE: 4.2% at 420 nm, STH: 0.1%	[5]
Pt/$SrTiO_3$:Cr/Ta	PtO_x/WO_3	IO_3^-/I^-	300 W Xe lamp (>420 nm)	H_2O	AQE: 0.1% at 420 nm	[6]
Pt/TaON	PtO_x/WO_3	IO_3^-/I^-	300 W Xe lamp (>420 nm)	H_2O	AQE: 0.4% at 420 nm	[7]
Pt/ZrO_2/TaON	PtO_x/WO_3	IO_3^-/I^-	300 W Xe lamp (>420 nm)	H_2O	AQE: 6.3% at 420 nm	[8]
Pt/$MgTa_2O_{6-x}N_y$/TaON	PtO_x/WO_3	IO_3^-/I^-	300 W Xe lamp (>420 nm)	H_2O	AQE: 6.8% at 420 nm	[9]
$Rh_yCr_{2-y}O_3$-ZrO_2/TaON	Au/CoO_x-$BiVO_4$	$[Fe(CN)_6]^{3-/4-}$	300 W Xe lamp (>420 nm)	H_2O (25 mM sodium phosphates, pH = 6.0)	AQE: 10.3% at 420 nm, STH: ~0.5%	[10]
$Rh_yCr_{2-y}O_3$-ZrO_2/TaON or $MgTaO_{6-x}N_y$/TaON	Ir/$FeCoO_x$-$BiVO_4$	$[Fe(CN)_6]^{3-/4-}$	300 W Xe lamp (>420 nm)	H_2O (25 mM sodium phosphates, pH = 6.0)	AQE: 12.3% at 420 nm, STH: ~0.6%	[11]
$Rh_yCr_{2-y}O_3$-ZrO_2/TaON or $MgTaO_{6-x}N_y$/TaON	Ir/$BiVO_4$	$[Fe(CN)_6]^{3-/4-}$	300 W Xe lamp (>420 nm)	H_2O (25 mM sodium phosphates, pH = 6.0)	AQE: 16.9% at 420 nm, STH: ~0.8%	This work

Supplemental Experimental Procedures

Chemicals

The Ta_2O_5 (99.9%, High Purity Chemicals), $ZrO(NO_3)_2\cdot 2H_2O$ (ZrO_2 45.0%, Guangfu Chemical Reagent), $MgSO_4$ (99.5%, Alfa Aesar), $Bi(NO_3)_3\cdot 5H_2O$ (99.0%, Sinopharm Chemical), NH_4VO_3 (99.0%, Sinopharm Chemical) and polyvinyl alcohol (PVA, Sigma-Aldrich, 99%) were used for the preparation of ZrO_2-modified TaON, $MgTa_2O_{6-x}N_y$/TaON composite and $BiVO_4$ samples. $Na_3RhCl_6\cdot 12H_2O$ (Rh 17.1%, Alfa Aesar), K_2CrO_4 (99.5% Kermal Chemical Reagent), K_2IrCl_6 (Ir: 39% Alfa Aesar), and $Na_3IrCl_6\cdot xH_2O$ (Sigma-Aldrich) were employed as the precursors of cocatalysts. Methanol (99.5%, Sinopharm Chemical) and $K_4[Fe(CN)_6]\cdot 3H_2O$ (99.5%, Sinopharm Chemical) were used as hole acceptors. $K_3[Fe(CN)_6]$ (99.5%, Sinopharm Chemical) were used as electron donors. All chemicals were used as-purchased without further purification.

Preparation of BVO electrodes

The BVO photoanode was prepared by referring to the previous work[12]. First of all, the precursor solution was prepared by dissolving $Bi(NO_3)_3\cdot 5H_2O$, NH_4VO_3 and polyvinyl alcohol in 60% HNO_3. Then it was spin-coated on the fluorine doped tin oxide (FTO). In order to get the BVO seed layer, the precursor solution was spin-coated on the FTO and then heated at 623 K for 2 h in the air. Secondly, the BVO precursor film solution was formed by dissolving $Bi(NO_3)_3\cdot 5H_2O$ and NH_4VO_3 in 2.0 M HNO_3 and adjusting the pH to be about 0.9 with ammonia solution, meanwhile, the treated FTO was immersed. After that, the solution and as-prepared substrate was transferred to a Teflon-lined autoclave for hydrothermal treatment at 473 K for 12 h. Finally, the BVO photoanode film was calcined at 773 K for 4 h. The K_2IrCl_6 (10 μL, the concentration of solution: 1 mg mL^{-1}) solution was added on the surface of BVO photoanode and after drying it was treated at 473 K, 573 K, 673 K for 0.5 h under a flow of 5% H_2/Ar (200 mL min^{-1}) for the tests of surface photovoltage.

The method of measuring the photon number

The method of measuring the photon number for a specific single wavelength (top irradiation-type) is described as follows: First of all, the light intensity near the center of the circular spot was measured to find the point with the largest light intensity, which was then set up as the center of the circle (yellow dot in Scheme S1). Secondly, the number of photons at the top, bottom, left and right from the center (white dot in Scheme S1) with the interval of about 3 mm was separately measured for three times, and their average photon number was considered as the even photon number with this circle/ring area. Similar procedure and measurement were carried out for other circle with every diameter enhanced by 3 mm (as shown in Scheme S1: the dotted line represents the center of different rings and the average value of the four points represents the number of photons per point of the entire shadow circle/ring). Finally, the total photon number of the circle/ring is obtained through multiplying the circular/ring area and average photon number, and then the different circular/ring photon numbers are added to get the total number of photons under the irradiation area.

Basic characterizations of photocatalysts

X-ray diffraction (XRD) measurement was performed on a Rigaku D/Max-2500/PC powder diffractometer (Cu Kα radiation) with an operating voltage of 40 kV and current of 200 mA. The scan rate applied was 5° min^{-1} in the experimental range. UV-Vis diffuse reflectance spectra (DRS) was carried out on a UV-Vis spectrophotometer (JASCO V-550) equipped with an integrating sphere, and $BaSO_4$ powder was used as the reference for baseline correction. The morphologies were examined by field emission scanning electron microscopy (FESEM; S-5500, Hitachi) taken with a Quanta 200 FEG scanning electron microscope. High-resolution transmission electron microscopy (HRTEM) was carried out on a JEOL JEM-ARM200F microscope. The binding energies were determined by X-ray photoelectron spectroscopy (XPS, Thermo Esclab 250Xi, a monochromatic Al Kα X-ray source), and calibrated by the C 1s peak (284.6 eV) for each sample. Diffuse reflectance infrared Fourier transform (DRIFT) spectra were recorded with a VERTEX 80V spectrometer. For each CO adsorption measurement, the sample was pretreated to remove the adsorbed water molecules (heated at 473 K for 0.5 h under Ar atmosphere) and then *in situ* reduced with H_2 for 1 h at different temperature (473 K, 573 K, 673 K), followed by cooling to room temperature. The gas flow was then switched to Ar and held at this temperature for 0.5 h to collect the background spectrum. Then, CO was introduced into the system until reaching the saturated adsorption of CO. Subsequently, the system was purged with Ar to remove gaseous CO, following which the DRIFT spectrum of CO was collected in Kubelka-Munk mode. The lock-in-based surface photovoltage (SPV) spectroscopic measurement system consisted of a 500 W xenon lamp (LSH-X500, Zolix), a grating monochromator (Omni-5007, Zolix), a lock-in amplifer (SR830-DSP, Stanford) with a light chopper (SR540, Stanford), a photovoltaic cell, and a computer. Monochromatic light was provided by passing light from a 500 W xenon lamp through the grating monochromator. A low chopping frequency of 23 Hz was used in the conventional testing. And the measurements were carried out in air atmosphere at room temperature.

The X-ray photoemission electron microscopy (XPEEM) measurement

The Ir/BVO-573 sample was dispersed in ethanol solution and loaded on the indium tin oxides (IFO) glass by spin-coating. The element chemical-state-specific X-ray photoemission electron microscopy (XPEEM) measurement was conducted at the XPEEM endstation (BL09U, Dreamline) at the Shanghai Synchrotron Radiation Facility (SSRF) equipped with an aberration-corrected spectroscopic photoemission and low-energy electron microscopy system (SPELEEM III, ELMITEC GmbH). A 515 nm wavelength laser (2.4 eV, 1000 W cm^{-2}) was used to excite $BiVO_4$, which was the second harmonic of the Yb:KGM laser (1030 nm, pulse width less than 100 fs, 76 MHz, Flint, Light Conversion) from a lithium triborate (LBO) crystal. Measurements were carried out in an ultra-high vacuum chamber with a base pressure of 2×10^{-10} Torr or better. And the PEEM experiment was carried out at room temperature. In addition to PEEM imaging, LEEM (low-energy electron microscopy) imaging was also utilized to capture the topography of the sample surface and to spatially correlate the PEEM signatures.

The XPEEM utilized synchrotron radiation X-rays to achieve spatially resolved XPS. An X-ray photon energy of 350 eV was used to directly emit photoelectrons from atomic core levels, which were then imaged by PEEM. The energy-filtered XPEEM images were recorded in a stack by scanning the kinetic energy of core-level photoelectrons within a narrow kinetic energy window for the interested ranges, such as Ir $4f_{5/2}$. Spatially resolved XPS spectra were obtained by extracting the photoelectron intensities from different facets in the stacked XPEEM images.

Single-Particle photoluminescene (PL) measurements

The BVO, Ir/BVO-573 and Ir(P.I.)/BVO-573 samples were centrifuged at 8000 rpm for 5 min and wash with ethanol. Then it was diluted (1:3) with MilliQ ultrapure water. The well dispersed aqueous suspensions of NPs were spin-coated on the cleaned quartz cover glass. A scanning confocal microscope system (PicoQuant, MicroTime 200) coupled with an Olympus IX73 inverted fluorescence microscope was used to obtain single-particle PL images and spectrum. The nanoparticles were excited through an oil-immersion objective lens (Olympus, UplanSApochromat, 100× , 1.4 NA) with a 405 nm continuous wave (CW) laser controlled by a PDL-800B driver (PicoQuant). To obtain single-particle of PL images and spectrum, the intensity of laser was set to 0.05 mW.

Single-particle SRSPS (spatially resolved surface photovoltage spectroscopy) measurement

The Ir/BVO-573 sample was deposited on the FTO by the particle transfer method[13]. The contact potential difference (CPD) of the sample was measured using Kelvin probe force microscopy (KPFM, Bruker Dimension Fastscan) under ambient atmosphere in amplitude-modulated mode. The lift mode was used with a height of 100 nm for SPV. In lift mode, the topography and CPD signals were sequentially recorded. The Pt/Ir-coated Sb-doped Si tip (SCM-PIT-V2) was used as a Kelvin tip. A blue LED (λ = 405 nm, 0.2 mW cm^{-2}) almost parallel to the substrate was used to measure the CPD under illumination. The difference of the surface potential mapping under dark and light conditions in the same locations was extracted as the surface photovoltage image.

SPV is the difference between the CPD values obtained before and after illumination. The formula can be expressed as $\mathrm{SPV} = \mathrm{CPD}_{\mathrm{light}} - \mathrm{CPD}_{\mathrm{dark}}$[14]. The SPV magnitude is directly proportional to the number of separated charges and the SPV sign reflects the types of surface photogenerated charge. The positive sign denotes the photogenerated holes and negative sign denotes the photogenerated electrons[15].

Supplemental References

1. Abe, R., Shinmei, K., Koumura, N., Hara, K., and Ohtani, B. (2013). Visible-light-induced water splitting based on two-step photoexcitation between dye-sensitized layered niobate and tungsten oxide photocatalysts in the presence of a triiodide/iodide shuttle redox mediator. J. Am. Chem. Soc. *135*, 16872–16884. 10.1021/ja4048637.
2. Sasaki, Y., Kato, H., and Kudo, A. (2013). $[Co(bpy)_3]^{3+/2+}$ and $[Co(phen)_3]^{3+/2+}$ electron mediators for overall water splitting under sunlight irradiation using Z-scheme photocatalyst system. J. Am. Chem. Soc. *135*, 5441–5449. 10.1021/ja400238r.
3. Kato, H., Hori, M., Konta, R., Shimodaira, Y., and Kudo, A. (2004). Construction of Z-scheme type heterogeneous photocatalysis systems for water splitting into H_2 and O_2 under visible light irradiation. Chem. Lett. *33*, 1348–1349. 10.1246/cl.2004.1348.
4. Fujito, H., Kunioku, H., Kato, D., Suzuki, H., Higashi, M., Kageyama, H., and Abe, R. (2016). Layered perovskite oxychloride Bi_4NbO_8Cl: A stable visible light responsive photocatalyst for water splitting. J. Am. Chem. Soc. *138*, 2082–2085. 10.1021/jacs.5b11191.
5. Kato, H., Sasaki, Y., Shirakura, N., and Kudo, A. (2013). Synthesis of highly active rhodium-doped $SrTiO_3$ powders in Z-scheme systems for visible-light-driven photocatalytic overall water splitting. J. Mater. Chem. A *1*, 12327–12333. 10.1039/c3ta12803b.
6. Sayama, K., Mukasa, K., Abe, R., Abe, Y., and Arakawa, H. (2001). Stoichiometric water splitting into H_2 and O_2 using a mixture of two different photocatalysts and an IO_3^-/I^- shuttle redox mediator under visible light irradiation. Chem. Commun. *23*, 2416–2417. 10.1039/b107673f.
7. Abe, R., Takata, T., Sugihara, H., and Domen, K. (2005). Photocatalytic overall water splitting under visible light by TaON and WO_3 with an IO_3^-/I^- shuttle redox mediator. Chem. Commun. *30*, 3829–3831. 10.1039/b505646b.
8. Maeda, K., Higashi, M., Lu, D., Abe, R., and Domen, K. (2010). Efficient nonsacrificial water splitting through two-step photoexcitation by visible light using a modified oxynitride as a hydrogen evolution photocatalyst. J. Am. Chem. Soc. *132*, 5858–5868. 10.1021/ja1009025.
9. Chen, S., Qi, Y., Hisatomi, T., Ding, Q., Asai, T., Li, Z., Ma, S. S. K., Zhang, F., Domen, K., and Li, C. (2015). Efficient visible-light-driven Z-scheme overall water splitting using a $MgTa_2O_{6-x}N_y$/TaON heterostructure photocatalyst for H_2 evolution. Angew. Chem. In. Ed. *54*, 8498–8501. 10.1002/anie.201502686.
10. Qi, Y., Zhao, Y., Gao, Y., Li, D., Li, Z., Zhang, F., and Li, C. (2018). Redox-based visible-light-driven Z-scheme overall water splitting with apparent quantum efficiency exceeding 10%. Joule *2*, 2393–2402. 10.1016/j.joule.2018.07.029.
11. Qi, Y., Zhang, J., Kong, Y., Zhao, Y., Chen, S., Li, D., Liu, W., Chen, Y., Xie, T., Cui, J., et al. (2022). Unraveling of cocatalysts photodeposited selectively on facets of $BiVO_4$ to boost solar water splitting. Nat. Commun. *13*, 484. 10.1038/s41467-022-28146-6.
12. Li, D., Liu, Y., Shi, W., Shao, C., Wang, S., Ding, C., Liu, T., Fan, F., Shi, J., and Li, C. (2019). Crystallographic-orientation-dependent charge separation of $BiVO_4$ for solar water oxidation. ACS Energy Lett. *4*, 825–831. 10.1021/acsenergylett.9b00153.
13. Wang, Q., Hisatomi, T., Jia, Q., Tokudome, H., Zhong, M., Wang, C., Pan, Z., Takata, T., Nakabayashi, M., Shibata, N., et al., (2016). Scalable water splitting on particulate photocatalyst sheets with a solar-to-hydrogen energy conversion efficiency exceeding 1%.

Nat. Mater. *15*, 611–615. 10.1038/NMAT4589.

14. Kronik, L., and Shapira, Y. (1999). Surface photovoltage phenomena: theory, experiment, and applications. Surf. Sci. Rep. *37*, 1–206. 10.1016/S0167-5729(99)00002-3.
15. Chen, R., Fan, F., Dittrich, T., and Li, C. (2018). Imaging photogenerated charge carriers on surfaces and interfaces of photocatalysts with surface photovoltage microscopy. Chem. Soc. Rev. *47*, 8238–8262. 10.1039/c8cs00320c.